

**AFRL-RD-PS-  
TR-2016-0003**

**AFRL-RD-PS-  
TR-2016-0003**

**TIME-DOMAIN FINITE ELEMENT ANALYSIS OF  
NONLINEAR BREAKDOWN PROBLEMS IN HIGH-  
POWER-MICROWAVE DEVICES AND SYSTEMS**

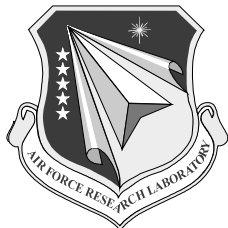
**Su Yan and Jian-Ming Jin**

**University of Illinois  
Center for Computational Electromagnetics  
Department of Electrical and Computer Engineering  
Urbana, IL 61801**

**24 December 2015**

**Final Report**

**APPROVED FOR PUBLIC RELEASE; DISTRIBUTION IS UNLIMITED.**



**AIR FORCE RESEARCH LABORATORY  
Directed Energy Directorate  
3550 Aberdeen Ave SE  
AIR FORCE MATERIEL COMMAND  
KIRTLAND AIR FORCE BASE, NM 87117-5776**

## **NOTICE AND SIGNATURE PAGE**

Using Government drawings, specifications, or other data included in this document for any purpose other than Government procurement does not in any way obligate the U.S. Government. The fact that the Government formulated or supplied the drawings, specifications, or other data does not license the holder or any other person or corporation; or convey any rights or permission to manufacture, use, or sell any patented invention that may relate to them.

Qualified requestors may obtain copies of this report from the Defense Technical Information Center (DTIC) (<http://www.dtic.mil>).

AFRL-RD-PS-TR-2016-0003 HAS BEEN REVIEWED AND IS APPROVED FOR PUBLICATION IN ACCORDANCE WITH ASSIGNED DISTRIBUTION STATEMENT.

//ANDREW GREENWOOD//

---

ANDREW GREENWOOD, DR-IV  
Project Officer

//MARY LOU ROBINSON//

---

MARY LOU ROBINSON, DR-IV  
Chief, High Power Electromagnetics Division

This report is published in the interest of scientific and technical information exchange, and its publication does not constitute the Government's approval or disapproval of its ideas or findings.

# REPORT DOCUMENTATION PAGE

*Form Approved  
OMB No. 0704-0188*

Public reporting burden for this collection of information is estimated to average 1 hour per response, including the time for reviewing instructions, searching existing data sources, gathering and maintaining the data needed, and completing and reviewing this collection of information. Send comments regarding this burden estimate or any other aspect of this collection of information, including suggestions for reducing this burden to Department of Defense, Washington Headquarters Services, Directorate for Information Operations and Reports (0704-0188), 1215 Jefferson Davis Highway, Suite 1204, Arlington, VA 22202-4302. Respondents should be aware that notwithstanding any other provision of law, no person shall be subject to any penalty for failing to comply with a collection of information if it does not display a currently valid OMB control number. **PLEASE DO NOT RETURN YOUR FORM TO THE ABOVE ADDRESS.**

<b>1. REPORT DATE (DD-MM-YYYY)</b> 24-12-2015	<b>2. REPORT TYPE</b> Final Report	<b>3. DATES COVERED (From - To)</b> 24-09-2014 – 24-11-2015 <b>5a. CONTRACT NUMBER</b> <b>5b. GRANT NUMBER</b> FA9451-14-1-0349 <b>5c. PROGRAM ELEMENT NUMBER</b> 62604F <b>5d. PROJECT NUMBER</b> 4867HM14 <b>5e. TASK NUMBER</b> HM EF126469 <b>5f. WORK UNIT NUMBER</b> D08D		
<b>4. TITLE AND SUBTITLE</b>  Time-Domain Finite Element Analysis of Nonlinear Breakdown Problems in High-Power Microwave Devices and Systems				
<b>6. AUTHOR(S)</b> Su Yan and Jian-Ming Jin				
<b>7. PERFORMING ORGANIZATION NAME(S) AND ADDRESS(ES)</b>  University of Illinois Center for Computational Electromagnetics Department of Electrical and Computer Engineering Urbana, IL 61801		<b>8. PERFORMING ORGANIZATION REPORT NUMBER</b>		
<b>9. SPONSORING / MONITORING AGENCY NAME(S) AND ADDRESS(ES)</b>  Air Force Research Laboratory 3550 Aberdeen Avenue SE Kirtland AFB, NM 87117-5776		<b>10. SPONSOR/MONITOR'S ACRONYM(S)</b> AFRL/RDHE  <b>11. SPONSOR/MONITOR'S REPORT NUMBER(S)</b> AFRL-RD-PS-TR-2016-0003		
<b>12. DISTRIBUTION / AVAILABILITY STATEMENT</b> Approved for public release: distribution unlimited.				
<b>13. SUPPLEMENTARY NOTES</b> OPS-15-9285				
<b>14. ABSTRACT</b>  This final report describes the effort to develop a highly accurate and efficient simulation tool for the multi-physics and multiscale modeling and simulation of the electromagnetic-plasma interaction and the high-power microwave breakdown in air. Under the high pressure and high frequency condition of the high-power air breakdown, the physical phenomenon is described using a nonlinearly coupled full-wave Maxwell and fluid plasma system. This nonlinear system is then solved by a numerical method that is uniformly high order in both space and time. Accurate and efficient numerical simulation methods and techniques are introduced, developed, and validated. Several numerical examples are given to demonstrate the capability of the numerical method in the modeling and simulation of the high-power microwave air breakdown problems, where the underlining physical process can be well understood and interpreted from the simulation results.				
<b>15. SUBJECT TERMS</b> High power microwave, time-domain, finite-element, discontinuous-Galerkin, nonlinear breakdown				
<b>16. SECURITY CLASSIFICATION OF:</b>		<b>17. LIMITATION OF ABSTRACT</b> SAR	<b>18. NUMBER OF PAGES</b> 50	<b>19a. NAME OF RESPONSIBLE PERSON</b> Andrew Greenwood
<b>a. REPORT</b> Unclassified	<b>b. ABSTRACT</b> Unclassified	<b>c. THIS PAGE</b> Unclassified		<b>19b. TELEPHONE NUMBER (include area code)</b>

This page intentionally left blank.

## TABLE OF CONTENTS

Section	Page
List of Figures .....	iv
List of Tables .....	vi
1.0 SUMMARY .....	1
2.0 INTRODUCTION .....	1
3.0 METHODS, ASSUMPTIONS, PROCEDURES .....	3
3.1 Physical Model and Its Challenges .....	3
3.1.1 Plasma Fluid Model.....	3
3.1.2 Coupled Electromagnetic-Plasma System.....	6
3.1.3 Multi-Physics and Multiscale Challenges .....	7
3.2 Numerical Scheme .....	9
3.3 Mathematical Basics and Considerations .....	10
3.3.1 Nodal Discontinuous-Galerkin Time-Domain Method.....	10
3.3.2 Higher-Order Spatial Discretization.....	15
3.3.3 Higher Order Temporal Discretization.....	20
3.4 Computational Acceleration Techniques.....	22
3.4.1 Dynamic $p$ -Adaption .....	22
3.4.2 GPU Acceleration.....	23
4.0 RESULTS AND DISCUSSION.....	24
4.1 Validation of the LDG Method for the Diffusion Equation.....	24
4.2 Modeling of Plasma Shielding of the Electromagnetic Wave .....	26
4.2.1 Physics Involved.....	26
4.2.2 Numerical Settings .....	26
4.2.3 Numerical Results and Analysis.....	27
4.3 Reproduction of the Microwave Streamer .....	32
4.3.1 Physics Involved.....	32
4.3.2 Numerical Settings .....	33
4.3.3 Numerical Results and Analysis.....	34
5.0 CONCLUSIONS .....	37
6.0 REFERENCES .....	38

## LIST OF FIGURES

<b>Figure</b>	<b>Page</b>
Figure 1. Spatial Variation of the Incident Electric Field (a), Initial Electron Density Distribution (b), Secondary Electric (c) and Magnetic (d) Fields Produced by the Electron Plasma Current. Only 1/4 of the Solution Domain (A Spherical Region Filled With Air) Is Shown Because of Symmetry .....	9
Figure 2. Optimized Interpolating Nodes in Tetrahedron [19]. (a) $p = 1$ , (b) $p = 2$ , (c) $p = 4$ , (d) $p = 6$ , (e) $p = 8$ , and (f) $p = 10$ .....	18
Figure 3. (a) Spectral Radius of the Facial Matrix Versus Polynomial Basis Order; (b) Time Step Size Required to Maintain Stability Versus Polynomial Basis Order. The Time Step Sizes Are Normalized Against That of the First-Order Orthonormal Basis Function.....	19
Figure 4. Contour Plot of the Electron Density (Left Half) and it's Gradient (Right Half).....	23
Figure 5. Comparison between the Numerical and the Analytical Solutions of the Diffusion Equation .....	25
Figure 6. Contour Plot of the Density Distribution at the Final Time Step .....	26
Figure 7. Illustration of the Solution Domain of the Microwave Breakdown Problem in a Metallic Aperture.....	27
Figure 8. Temporal Response of the Electric Fields Recorded at P1 and P2 in (a) the Vacuum and (b) the Air Cases.....	28
Figure 9. (a) Comparison of the Temporal Response of the Electric Fields Recorded at P2 in Both Cases; (b) Temporal Evolution of the Electron Density Recorded at P1 in the Air Case ..	28
Figure 10. Electron Density Distribution in the Air Aperture at 0.28 ns. (a) One Dimensional Distribution Along y Direction; (b) One Dimensional Distribution Along z Direction; (c) Two Dimensional Snapshot.....	29
Figure 11. Snapshots of the Time Evolution of the Electron Density and the Effective Electric Field in the Air Aperture at (a) 0.28 ns, (b) 0.32 ns, (c) 0.36 ns, (d) 0.40 ns, (e) 0.44 ns, (f) 0.48 ns, (g) 0.52 ns, (h) 0.56 ns, (i) 0.60 ns, and (j) 4.00 ns, Respectively .....	31
Figure 12. The Microwave Streamer Discharge Recorded in Experiments. Streamer Discharges in Air at (a) 480 torr and (b) 760 torr. Streamer Discharges in Hydrogen at (c) 480 torr and (d) 1000 torr [42] .....	32
Figure 13. Effective Ionization Frequency and Electron Diffusion Coefficient as Functions of Effective Field .....	33
Figure 14. The Initial Condition of the Electron Distribution, a Gaussian Dot .....	33
Figure 15. The Spatial and Temporal Evolution of the Microwave Streamer at (a) 0.0 ns, (b) 12.0 ns, (c) 14.0 ns, and (d) 15.8 ns, Respectively. In Each Set of Plot, the Upper Two Figures Show the Electron Density and the Effective Field Distributions in a 2D Cut, and the Lower Two Figures Show the Corresponding Distributions as 1D Curves Along the Center Line (the Symmetric Axis) .....	35
Figure 16. (a) Electron Density, (b) Secondary Electric Field Distribution, and (c) Combination View of the Electron Density and the Secondary Electric Field Generated by the Electron Plasma at 15.8 ns .....	36
Figure 17. The (a) y and (b) z Components of the Secondary Electric Field Radiated by the Electron Plasma at 15.8 ns, Which Demonstrate the Field Continuity in all Directions Throughout the Simulation Domain. The x Component is Zero in the Plane of Observation and is Not Shown .....	37

Figure 18. Dynamic  $p$ -Adaption During Simulation. The Upper Half of the Two Figures Show the Polynomial Orders in the Computational Domain, the Lower Left and Lower Right of the Two Figures are the Electron Density and Electric Field Magnitude, Respectively. (a) 0.0 ns; (b) 15.8 ns ..... 37

## LIST OF TABLES

<b>Table</b>	<b>Page</b>
Table 1. Characteristics of the Multiscale Physics .....	8

## **1.0 SUMMARY**

This final report describes the effort to develop a highly accurate and efficient simulation tool for the multi-physics and multiscale modeling and simulation of the electromagnetic-plasma interaction and the high-power microwave breakdown in air. Under the high pressure and high frequency condition of the high-power air breakdown, the physical phenomenon is described using a nonlinearly coupled full-wave Maxwell and fluid plasma system. This nonlinear system is then solved by a numerical method that is uniformly high order in both space and time. Accurate and efficient numerical simulation methods and techniques are introduced, developed, and validated. Several numerical examples are given to demonstrate the capability of the numerical method in the modeling and simulation of the high-power microwave air breakdown problems, where the underlining physical process can be well understood and interpreted from the simulation results.

## **2.0 INTRODUCTION**

High-power microwave (HPM) devices and systems have very important civilian and military applications. To design better HPM devices that generate higher electromagnetic power and longer pulse width, extensive research effort has been devoted to the development of microwave sources [1][2], the design of output windows [3][4], and the optimization of advanced cathodes. However, as the power density goes higher and higher, the HPM devices and systems are more and more vulnerable to the HPM breakdown, including the air breakdown during the generation and transmission of HPM and the dielectric window breakdown when the HPM is radiating through the dielectric window. When breakdown happens, the transmission capability of a microwave device can be severely limited.

The HPM breakdown can occur inside the HPM device and on the output window due to surface flashover phenomena [5]-[7] and multipactor [8][9]. During the HPM generation and radiation, the electrons in the HPM device are accelerated by the high-intensity electromagnetic fields. The motion of electrons produces impact on other gas particles or metal and dielectric surfaces, which can release secondary electrons into the device. These electrons are then accelerated by the electromagnetic fields and also impact other particles or surfaces. Meanwhile, they also generate secondary electromagnetic fields and enhance the original fields. If the power density is sufficiently high, the free electrons can sustain themselves through the electromagnetic fields they generate, and therefore, result in an exponential multiplication of the electrons, which is known as breakdown. This may lead to the malfunction or even damage of the HPM devices and systems. To achieve a better understanding of the breakdown mechanism and process and to improve the design of microwave devices, research investigation has been conducted, both experimentally [3][4] and computationally [10][11]. By comparing the numerical results obtained from numerical simulations with experimental observations, breakdown theories can be validated and the underlying physics can be better understood. In order to simulate such a multi-physics process involving field-particle interaction and strong nonlinearity with a high accuracy and reliability, both the electromagnetic physics and the plasma physics have to be described, modeled, and solved accurately.

Governed by Maxwell's equations, the electromagnetic fields can be solved with various numerical methods developed by the computational electromagnetics community. Among all the methods, the finite-difference time-domain (FDTD) method is most widely used because of its

simplicity and high efficiency. Also because of its scalar representation of each field component on structured mesh grids, the continuity of the electromagnetic fields can be preserved, which is especially important when the electromagnetic fields are coupled to the particle motion. However, the stair-case approximation of the solution domain, the finite-difference approximation of the fields and their derivatives, and the explicit leap-frog time-marching scheme used in the FDTD method result in a low-order accuracy, which requires an extremely dense mesh grid and an extremely tiny time step size in a simulation to achieve a desired accuracy. On the contrary, another widely used method, the finite-element time-domain (FETD) method [12], which employs an unstructured mesh for the geometric discretization, high-order vector basis functions for the field expansion, and implicit time-marching scheme, is able to achieve high-order accuracy and unconditional stability. Unfortunately, the implicit scheme results in a globally coupled system that has to be solved at every time step, which leads to a reduced efficiency compared to the FDTD method. More importantly, because of the application of the vector basis functions, only the field components that are tangential to the elemental interfaces are continuous, and those that are normal to the interfaces are much less accurate. When coupled with the particle solver, the discontinuous normal components of the fields will impose an unpredictable amount of force to the particles and result in a spurious solution or even a numerical breakdown of the simulation. To overcome the abovementioned issues of both methods, in this work the nodal discontinuous Galerkin time-domain (DGTD) method [13]-[19] is employed to solve for the electromagnetic fields. Different from the vector DGTD [20][21] traditionally used in the computational electromagnetics community, the nodal DGTD method employs nodal interpolatory basis functions to represent the physical quantities, which guarantees the field continuity in all three spatial directions. Using an unstructured mesh, high-order nodal basis functions, and an explicit high order time-marching scheme, the nodal DGTD method is able to achieve high-order accuracy in the geometric discretization of the solution domain and in the spatial and the temporal discretization of the field solution. In addition, the nodal DGTD method also enjoys the following advantages: (1) high parallel efficiency on a massively parallel platform; and (2) high flexibility and efficiency by using dynamic *hp*-adaption and local time-stepping scheme.

The other half of the physical phenomenon, the plasma physics [22][23], can be described by the Vlasov and the Boltzmann equations in the collision-less and the collisional cases, respectively. Because of the high dimensionality of the Vlasov and the Boltzmann equations and the consequent difficulty in their direct solution, various simplified models are usually used, where in the low to moderate pressure and density case, the well-known particle-in-cell (PIC) method has been widely adopted in the simulation of high-power microwave devices, and in the high pressure and density case, fluid models work adequately to describe the plasma behavior. In the case of air breakdown under atmosphere condition, fluid models can be adopted. By taking the first several moments of the Vlasov or the Boltzmann equation, a hierarchy of models can be obtained, from the simplest two-moments drift-diffusion model [24], to the three-moments hydrodynamic model [25], to the four-moments energy transport model [26][27], to the six-moments model [28], and so on. With the inclusion of higher order moments, more physical mechanisms are accounted for by the more sophisticated model. These models govern plasma quantities such as the plasma density, velocity, temperature, and energy. Since the related plasma parameters, such as ionization frequency, collision frequency, attachment frequency, and electron energy loss frequency, become highly nonlinear when the electromagnetic field intensity

is sufficiently high, the resultant coupled system also becomes highly nonlinear. Such a strong nonlinearity experienced in HPM devices inhibits the current computational methods from simulating the breakdown process accurately and efficiently. As a result, the major techniques used to increase the breakdown threshold in HPM devices and systems are still empirical.

In this work, the nodal DGTD is used to simulate both the electromagnetic physics and the plasma physics. In Section 3.0, the physical model and its challenge to the numerical methods will first be introduced, and the proposed numerical scheme and techniques will be described in detail. Several numerical examples will be presented in Section 0, and conclusion will be drawn in Section 0.

### 3.0 METHODS, ASSUMPTIONS, PROCEDURES

#### 3.1 Physical Model and Its Challenges

##### 3.1.1 Plasma Fluid Model

The plasma model adopted in this work is a simple drift-diffusion model that was originally developed in [29]-[33]. Starting from the Boltzmann equation (general form)

$$\frac{\partial f}{\partial t} + \mathbf{v} \cdot \nabla f + \frac{\mathbf{F}}{m} \cdot \nabla_{\mathbf{v}} f = \left( \frac{\partial f}{\partial t} \right)_{\text{coll}} \quad (1)$$

where  $f = f(\mathbf{r}, \mathbf{v}, t)$  stands for the seven-dimensional probability distribution function (PDF) of a single particle species, with the seven-dimensional phase space spanned by  $(\mathbf{r}, \mathbf{v}, t)$ ,  $\mathbf{F}$  stands for the force presented to the particle with a mass  $m$ , the term on the right-hand-side (RHS) stands for the collision mechanism. In the fluid model, the macroscopic concepts are defined by integrating the PDF over the velocity dimensions, which yields the definition of the particle density

$$n(\mathbf{r}, t) = \int f(\mathbf{r}, \mathbf{v}, t) d\mathbf{v} \quad (2)$$

the mean velocity

$$\mathbf{u} = \langle \mathbf{v} \rangle = \frac{1}{n} \int \mathbf{v} f(\mathbf{r}, \mathbf{v}, t) d\mathbf{v} \quad (3)$$

and the mean energy

$$\mathcal{E} = \frac{m}{2} \langle \mathbf{v}^2 \rangle = \frac{m}{2n} \int \mathbf{v}^2 f(\mathbf{r}, \mathbf{v}, t) d\mathbf{v} \quad (4)$$

of the particle species under consideration.

The basic conservation laws of the plasma physics can be derived by taking the first three moments of the Boltzmann equation, which results in the mass conservation equation (aka the particle continuity equation)

$$\frac{\partial n}{\partial t} + \nabla \cdot (n\mathbf{u}) = S \quad (5)$$

with  $S$  being the source term, the momentum conservation equation

$$\frac{\partial n\mathbf{u}}{\partial t} + \nabla \cdot (n\mathbf{u}\mathbf{u}) = -\frac{1}{m}\nabla \cdot \bar{\mathbf{P}} + n\frac{\mathbf{F}}{m} + \mathbf{R} \quad (6)$$

and the energy conservation equation

$$\frac{\partial n\mathcal{E}}{\partial t} + \nabla \cdot (n\mathbf{u}\mathcal{E} + \bar{\mathbf{P}} \cdot \mathbf{u} + \mathbf{Q}) = n\mathbf{u} \cdot \mathbf{F} + S_{\mathcal{E}} \quad (7)$$

respectively.

In the case of high-power microwave breakdown in air, the following reasonable assumptions can be made. (1) The pressure tensor is  $\bar{\mathbf{P}}$  is diagonal and isotropic, hence, is a scalar. (2) Since the discharge takes place at high pressure, the high collision condition can be assumed. (3) Local equilibrium between electric acceleration (energy gain from the electric field) and collisional momentum and energy loss is assumed, so that the ionization frequencies depend only on the local electric field. This is known as the local field approximation. Under these assumptions, one can end up with the drift-diffusion equation

$$\frac{\partial n}{\partial t} + \nabla \cdot (\pm \mu n\mathbf{E} - D\nabla n) = S \quad (8)$$

where  $\mu$  is the mobility coefficient and  $D$  is the diffusion coefficient. Since the breakdown under consideration takes place at microwave frequencies, the drift term zeros out over a full period of the electromagnetic wave, and therefore, can be ignored. As a result, the diffusion mechanism dominates over the drift mechanism in the microwave frequency range. Under the quasi-neutral assumption of the plasma, and taking into account of the ionization, attachment, and recombination effects, the drift-diffusion equation finally becomes

$$\frac{\partial n}{\partial t} = \nabla \cdot (D_{\text{eff}}\nabla n) + (v_i - v_a)n - r_{ei}n^2 \quad (9)$$

where  $D_{\text{eff}}$  is an effective diffusion coefficient,  $v_i$  and  $v_a$  are the ionization and the attachment frequencies, respectively, and  $r_{ei}$  is the electron-ion recombination coefficient.

In the above equation, the effective diffusion coefficient  $D_{\text{eff}}$  is a combination of the free electron diffusion coefficient  $D_e$  and the plasma bulk ambipolar diffusion coefficient  $D_a$

$$D_{\text{eff}} = \frac{\alpha D_e + D_a}{\alpha + 1} \quad (10)$$

where  $\alpha$  is a weighting parameter given by

$$\alpha = v_i \tau_M = \lambda_D^2 / L^2 \quad (11)$$

with  $\tau_M = \epsilon_0 / [en(\mu_e + \mu_i)]$  standing for the local dielectric (Maxwell) relaxation time,  $\epsilon_0$  being the vacuum permittivity, and  $\mu_e = e/m_e v_m$  and  $\mu_i = \mu_e/200$  being the electron and ion mobility, respectively. The local Debye length  $\lambda_D$  and the characteristic diffusion length  $L$  are given by ( $k_B$  is the Boltzmann constant, and  $T_e$  is the electron temperature)

$$\lambda_D = \sqrt{\epsilon_0 k_B T_e / e^2 n} \quad (12)$$

and

$$L = \|\nabla n/n\|^{-1} = \sqrt{D_e/v_i} \quad (13)$$

respectively. Around the edge of the plasma bulk, since the electron density drops quickly from a high level to almost zero, the electrons in this region diffuse with the electron free diffusion coefficient

$$D_e = \mu_e \frac{k_B T_e}{e} \quad (14)$$

In the plasma bulk, because of the presence of both electrons and ions, the much slower ambipolar diffusion is the dominant mechanism. Since the ions are much heavier than the electrons, the ion diffusion coefficient is very small and is usually ignored

$$D_i = \mu_i \frac{k_B T_i}{q_i} \approx 0. \quad (15)$$

The ambipolar diffusion coefficient, as a combination of the electron and the ion diffusion coefficients, is hence given by

$$D_a = \frac{\mu_i D_e + \mu_e D_i}{\mu_i + \mu_e} \approx \frac{\mu_i}{\mu_e} D_e = \mu_i \frac{k_B T_e}{e} \quad (16)$$

since  $\mu_e \gg \mu_i$  and  $D_e \gg D_i$ . To calculate both the electron and the ambipolar diffusion coefficients, the electron temperature needs to be obtained, which is usually expressed by an empirical relation between the electron temperature  $T_e$  and the effective field  $E_{\text{eff}}$  (will be defined in Section 3.2)

$$\frac{k_B T_e}{e} = \left[ 2.1 \times 10^{-3} \frac{E_{\text{eff}}}{p} \left( 91.0 + \frac{E_{\text{eff}}}{p} \right) \right]^{\frac{1}{3}}. \quad (17)$$

Other important physical mechanisms include ionization, attachment, and recombination. The ionization and attachment frequencies are usually combined as the effective ionization frequency  $v_{\text{eff}}$  which can be expressed in terms of the electron drift velocity  $v_d$

$$v_{\text{eff}} = v_i - v_a = \alpha v_d \quad (18)$$

$$v_d = \mu_e E \quad (19)$$

where  $\alpha$  is the ionization coefficient which characterizes the number of ionization events that an electron undergoes per unit length along the field and is given by the following empirical expression

$$\alpha = A_0 p [\exp^{-B_0(p/E_{\text{eff}}-p/E_c)} - 1] \quad (20)$$

if  $E_{\text{eff}}/p < 50$  (V/cm.torr), and

$$\alpha = A p \exp^{-B p/E_{\text{eff}}} \quad (21)$$

if  $E_{\text{eff}}/p \geq 50$  (V/cm.torr). In the above expressions,  $A_0 = 0.005$  ( $\text{cm}^{-1}\text{torr}^{-1}$ ),  $B_0 = 200$  (V/cm.torr), and  $E_c/p = 31.25$  (V/cm.torr), where  $E_c$  stands for the critical field intensity beyond which the ionization will dominant over attachment. In air, the coefficients  $A = 8.805$  ( $\text{cm}^{-1}\text{torr}^{-1}$ ),  $B = 258.45$  (V/cm.torr) when  $50 \leq E_{\text{eff}}/p \leq 200$  (V/cm.torr), and  $A = 15$  ( $\text{cm}^{-1}\text{torr}^{-1}$ ),  $B = 265$  (V/cm.torr) when  $100 \leq E_{\text{eff}}/p \leq 800$  (V/cm.torr).

To complete the description of the plasma, another equation that governs the particle velocity is needed. From the momentum conservation equation, by assuming that the distance travelled over one field period is small compared to the length scale of the field and pressure variation, one can obtain the kinetic equation

$$\frac{\partial \mathbf{u}}{\partial t} = \frac{q}{m} \mathbf{E} - v_m \mathbf{u} \quad (22)$$

where  $q$  is the charge carried by a particle, and  $v_m$  is the momentum transfer electron-neutral collision frequency, which is often assumed to have a simple relation with the pressure, for example

$$\frac{v_m}{p} = 5.3 \times 10^9 \text{ s}^{-1}\text{torr}^{-1} \text{ (in air).} \quad (23)$$

### 3.1.2 Coupled Electromagnetic-Plasma System

The interaction between the electromagnetic waves and the plasma fluid is governed by the coupled electromagnetic-plasma system, where the electromagnetic physics is described and

governed by Maxwell's equations, while the plasma physics is described and governed by the electron diffusion equation with the electron-neutral collision, ionization, attachment, and recombination mechanisms taken into consideration. With the conduction current expressed as  $\mathbf{J}_c = en\mathbf{u}$ , the coupled system is given by

$$\dot{\mathbf{H}} = -\frac{1}{\mu} \nabla \times \mathbf{E} \quad (24)$$

$$\dot{\mathbf{E}} = \frac{1}{\epsilon} (\nabla \times \mathbf{H} - \mathbf{J}_c) \quad (25)$$

$$\dot{\mathbf{J}}_c = -v_m \mathbf{J}_c + \frac{e^2 n}{m} (\mathbf{E} + \mathbf{E}^{inc}) \quad (26)$$

$$\dot{n} = \nabla \cdot (D_{eff} \nabla n) + (v_i - v_a)n - r_{ei}n^2. \quad (27)$$

Here, the scattered field formulation for Maxwell's equations is used in order to achieve a better numerical accuracy in the calculation of the secondary field radiated by the plasma fluid, which means the  $\mathbf{E}$  and  $\mathbf{H}$  in the formulation stand for the secondary (or scattered) field, with the superscript "sca" omitted for simplicity.

### 3.1.3 Multi-Physics and Multiscale Challenges

Physically speaking, the system described by the four governing equations is multiscale in nature. The multiscale nature of this system is not only in space but also in time. To understand such a multiscale problem, the characteristics of the electromagnetic and plasma physics are compared by taking into account the representative values of the physics involved in a typical application scenario.

For the spatial domain, the characteristic length of the electromagnetic physics is the wavelength, which is on the order of millimeter, for example, 3 mm at 100 GHz. The characteristic length of the plasma fluid is the Debye length  $\lambda_D$ , which can be as small as sub-micrometers. For example, for the electron plasma with an electron temperature of 2.0 eV, and an electron density on the order of  $10^{21}/m^3$ , the Debye length is on the order of 0.1  $\mu m$ .

For the temporal domain, the characteristic time of the electromagnetic physics is the period, which is on the order of picosecond, for example, 10 ps at 100 GHz. The characteristic time of the plasma fluid is determined by the diffusion and ionization mechanisms, which is on the order of nanoseconds. For example, under the same assumption for the electron temperature, and assume the magnitude of the incident electric field  $E = 5$  MV/m, and the atmosphere condition  $p = 760$  torr, for the plasma front (considered as free electrons) to propagate a distance of the characteristic diffusion length  $L = \|\nabla n/n\|^{-1}$ , at the estimated propagation velocity  $v = 2\sqrt{D_e v_i}$ , the characteristic time is estimated to be on the order of 1 ns.

The comparisons made here are summarized in Table 1. Clearly, for the spatial domain, the plasma fluid varies faster, but for the temporal domain, the electromagnetic wave varies faster. To design a good numerical algorithm that can solve the strongly coupled nonlinear electromagnetic-plasma system, both multiscale characteristics in space and time need to be considered and well addressed.

**Table 1. Characteristics of the Multiscale Physics**

	Electromagnetics	Plasma Fluid	Ratio	Fast Physics
Operating condition	$f = 100 \text{ GHz}$	$p = 760 \text{ torr}$ $k_B T_e = 2.0 \text{ eV}$ $n \sim 10^{21}/\text{m}^3$	--	--
Spatial characteristic	$\lambda = 3 \text{ mm}$	$\lambda_D = 0.1 \mu\text{m}$	$10^4: 1$	Plasma
Temporal characteristic	$T = 10 \text{ ps}$	$T = 1 \text{ ns}$	$1: 10^2$	Electromagnetics

From the above analysis, it seems that two different grids can be used in the spatial discretization of the two physics, where one coarser grid that resolves electromagnetic wavelength can be used for Maxwell's equation, and one denser grid that resolves the Debye length can be used for the electron diffusion equation. Unfortunately, it is not the case here. The reason is that the spatially fast varying electron density distribution and its resulting electron plasma current will produce a set of secondary electric and magnetic fields that are varying on the similar scale of the electron density distribution, which is much faster than the spatial variation of the incident fields. This can be observed very clearly from the figures in Figure 1, which depicts a typical application scenario where a 110-GHz high-power microwave incidents upon and interacts with a plasma bulk which has a Gaussian density distribution with a maximum value of  $10^{15}/\text{m}^3$  and a standard deviation of  $50 \mu\text{m}$ . Notice that in Figure 1(a), the wavelength is well resolved by the discretization grid depicted by white lines. However, with the same grid, the zoom-in plots shown in Figure 1(b)-(d) reveal the fact that the electron density, the secondary electric and magnetic fields are varying on the same spatial scale, and hence need to be resolved by the same resolution.

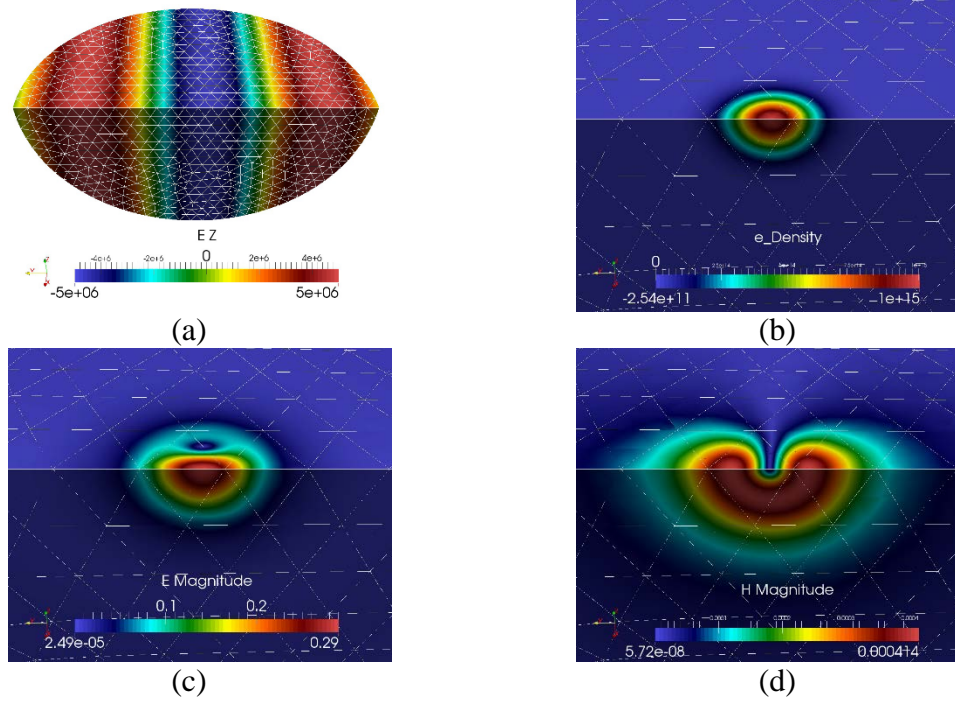


**Figure 1. Spatial Variation of the Incident Electric Field (a), Initial Electron Density Distribution (b), Secondary Electric (c) and Magnetic (d) Fields Produced by the Electron Plasma Current. Only 1/4 of the Solution Domain (A Spherical Region Filled With Air) Is Shown Because of Symmetry**

### 3.2 Numerical Scheme

In this section, the general numerical scheme is described, with all the mathematical details left for the next section.

With the physical nature and challenges of the problem well understood, a numerical scheme is designed for this problem. To begin, one single set of spatial grid is used for both electromagnetic and plasma physics. Since the grid cannot be extremely small to resolve the Debye length, higher order basis functions will be used in the numerical scheme to capture the fast variation of the physical quantities within each of the grid element. The use of the higher order basis functions can achieve higher order spatial accuracy without a dramatic increase of the total number of degrees of freedom (DoFs), which sets the numerical scheme used in this research apart from the FDTD method used in the past.

After the spatial discretization issue is addressed, the four partial differential equations (PDEs) that govern the coupled electromagnetic-plasma system are converted into four ordinary differential equations (ODEs) which can be integrated simultaneously in time to obtain the time-domain solution. However, because the aforementioned temporal multiscale nature of the physical problem, it is not necessary to solve all four equations simultaneously in time. Instead,

here we adopt a different solution strategy, which takes place in an iterative manner with each iteration containing two solution phases.

For the first phase, Maxwell's equations together with the momentum transfer equation are solved for one full period  $T$  with a time step size  $\Delta t_{\text{EM}}$  to obtain the root-mean-square (RMS) value of the electric field at every point  $\mathbf{r}$  in the solution domain

$$E_{\text{rms}}(\mathbf{r}) = \left( \frac{1}{T} \int_{t_0}^{t_0+T} \|\mathbf{E}(\mathbf{r}, t) + \mathbf{E}^{\text{inc}}(\mathbf{r}, t)\|^2 dt \right)^{1/2} \quad (28)$$

which is then used to calculate the effective electric field (with  $\omega$  being the angular frequency of the incident field)

$$E_{\text{eff}} = \frac{E_{\text{rms}}}{\sqrt{1 + \omega^2/v_m^2}} \quad (29)$$

and the reduced electric field  $E_{\text{eff}}/p$ . The reduced electric field is finally used to calculate the plasma parameters such as the ionization and attachment frequency  $v_i$  and  $v_a$ , and the plasma diffusion coefficient  $D_{\text{eff}}$  introduced in the preceding section, which are all functions of space and time, apparently.

Once all the plasma parameters are obtained at every point in the solution domain, the electron diffusion equation is solved for one time step with a time step size  $\Delta t_{\text{PL}} = T$ , which is the second phase in the iterative scheme. The newly obtained electron density  $n$  is then used in the momentum transfer equation for the first solution phase to continue for another period. The entire solution thus march on in time in an iterative manner.

It is worth mentioning that to make the entire numerical scheme uniformly high order accurate; the time integration scheme must also be high order accurate. To this end, the high-order explicit Runge-Kutta method is used in this work.

### 3.3 Mathematical Basics and Considerations

In this section, the mathematical formulation of the physical problem is described, with related mathematic basics and considerations given. To achieve the flexibility of geometric modeling, the high-order accuracy in both spatial and temporal discretization's, and more importantly, the continuity in all electromagnetic field components, the nodal DGTD method is employed to solve all four system equations given in the preceding section.

#### 3.3.1 Nodal Discontinuous-Galerkin Time-Domain Method

The nodal DGTD method used in this research work is different from the vector DG method used in computational electromagnetics community in a sense that the physical quantities are defined on each node (will be discussed in a following section), with the vector quantities

expanded into  $x$ ,  $y$ , and  $z$  components. The DGTD used in this work for Maxwell's equations and for electron diffusion equation are described below.

### 3.3.1.1 Nodal DGTD for the Hyperbolic PDE – Maxwell's Equations

As discussed before, Maxwell's equations need to be solved along with the momentum transfer equation for an entire period before the electron diffusion equation can be solved. Since the momentum transfer equation is valid point-wisely, there is no global coupling (information communication) involved in the solution. Here the discussion is focused on the solution of Maxwell's equations.

Consider Maxwell's equations

$$\dot{\mathbf{H}} = -\frac{1}{\mu} \nabla \times \mathbf{E} \quad (30)$$

$$\dot{\mathbf{E}} = \frac{1}{\epsilon} (\nabla \times \mathbf{H} - \mathbf{J}_c) \quad (31)$$

subject to the following boundary conditions

$$\hat{\mathbf{n}} \times \mathbf{E} = 0, \quad \hat{\mathbf{n}} \cdot \mathbf{H} = 0, \quad r \in \Gamma_{\text{PEC}} \quad (32)$$

$$\hat{\mathbf{n}} \times \mathbf{H} = 0, \quad \hat{\mathbf{n}} \cdot \mathbf{E} = 0, \quad r \in \Gamma_{\text{PMC}} \quad (33)$$

$$\hat{\mathbf{n}} \times \mathbf{E} + Z \hat{\mathbf{n}} \times \hat{\mathbf{n}} \times \mathbf{H} = 0, \quad \hat{\mathbf{n}} \times \mathbf{H} - Y \hat{\mathbf{n}} \times \hat{\mathbf{n}} \times \mathbf{H} = 0, \quad r \in \Gamma_{\text{ABC}} \quad (34)$$

where  $\Gamma_{\text{PEC}}$ ,  $\Gamma_{\text{PMC}}$ , and  $\Gamma_{\text{ABC}}$  denote the boundaries for the perfect electric conductor (PEC), the perfect magnetic conductor (PMC), and the absorbing boundary condition (ABC), respectively.

Testing the above equations with Lagrange polynomials  $\mathbf{l}_i = \hat{\mathbf{w}} l_i$  ( $\hat{\mathbf{w}} = \hat{\mathbf{x}}, \hat{\mathbf{y}}$ , or  $\hat{\mathbf{z}}$ ) on each tetrahedron element  $V_e$ , and applying the divergence theorem twice yield the strong form

$$\int_{V_e} \mathbf{l}_i \cdot \dot{\mathbf{H}} \, dV = -\frac{1}{\mu} \left[ \int_{V_e} \mathbf{l}_i \cdot \nabla \times \mathbf{E} \, dV + \oint_{\partial V_e} \mathbf{l}_i \cdot \hat{\mathbf{n}} \times (\mathbf{E}^* - \mathbf{E}) \, dS \right] \quad (35)$$

$$\int_{V_e} \mathbf{l}_i \cdot \dot{\mathbf{E}} \, dV = \frac{1}{\epsilon} \left[ \int_{V_e} \mathbf{l}_i \cdot \nabla \times \mathbf{H} \, dV + \oint_{\partial V_e} \mathbf{l}_i \cdot \hat{\mathbf{n}} \times (\mathbf{H}^* - \mathbf{H}) \, dS - \int_{V_e} \mathbf{l}_i \cdot \mathbf{J}_c \, dV \right] \quad (36)$$

where  $\mathbf{E}^*$  and  $\mathbf{H}^*$  are the numerical fluxes defined on the boundary faces of each tetrahedron element. Two choices of these numerical fluxes are commonly applied. One is the central flux, and the other is the upwind flux.

To facilitate the description, we define the average  $\{\cdot\}$  and jump  $[\![\cdot]\!]$  functions as follows

$$\{a\} = \frac{1}{2}(a^+ + a^-), \quad [\![a]\!] = a^+ - a^- \quad (37)$$

where the superscripts – and + indicate the inside and the outside of a surface, respectively. Note that the above definitions apply to both cases where  $a$  is a scalar or a vector variable.

- Central Flux

$$\mathbf{E}^* = \{\mathbf{E}\}, \quad \mathbf{H}^* = \{\mathbf{H}\} \quad (38)$$

- Upwind Flux

$$\mathbf{E}^* = \frac{1}{\{Y\}} \left( \{YE\} + \frac{1}{2} \hat{\mathbf{n}} \times [\![\mathbf{E}]\!] \right) \quad (39)$$

$$\mathbf{H}^* = \frac{1}{\{Z\}} \left( \{ZH\} - \frac{1}{2} \hat{\mathbf{n}} \times [\![\mathbf{H}]\!] \right) \quad (40)$$

Using either of the above numerical flux and expanding  $\mathbf{E}$  and  $\mathbf{H}$  in terms of  $p$ th order Lagrange polynomial basis functions

$$\mathbf{E} = \sum_{j=1}^{N_p} l_j (\hat{\mathbf{x}} E_{xj} + \hat{\mathbf{y}} E_{yj} + \hat{\mathbf{z}} E_{zj}), \quad \mathbf{H} = \sum_{j=1}^{N_p} l_j (\hat{\mathbf{x}} H_{xj} + \hat{\mathbf{y}} H_{yj} + \hat{\mathbf{z}} H_{zj}) \quad (41)$$

where  $N_p = \prod_{i=1}^d (p+i)/d!$  stands for the number of DoFs in a  $d$ -dimensional element, the strong form of the Maxwell's equations can be converted into the matrix form representation

$$M^e \dot{H}_x = -\frac{1}{\mu} (S_y^e E_z - S_z^e E_y + M_f^e F_x^E) \quad (42)$$

$$M^e \dot{H}_y = -\frac{1}{\mu} (S_z^e E_x - S_x^e E_z + M_f^e F_y^E) \quad (43)$$

$$M^e \dot{H}_z = -\frac{1}{\mu} (S_x^e E_y - S_y^e E_x + M_f^e F_z^E) \quad (44)$$

$$M^e \dot{E}_x = \frac{1}{\epsilon} (S_y^e H_z - S_z^e H_y + M_f^e F_x^H - M^e J_{cx}) \quad (45)$$

$$M^e \dot{E}_y = \frac{1}{\epsilon} (S_z^e H_x - S_x^e H_z + M_f^e F_y^H - M^e J_{cy}) \quad (46)$$

$$M^e \dot{E}_z = \frac{1}{\epsilon} (S_x^e H_y - S_y^e H_x + M_f^e F_z^H - M^e J_{cz}) \quad (47)$$

where the flux terms are given by

$$\mathbf{F}^E = \frac{1}{2} \hat{\mathbf{n}} \times [\![\mathbf{E}]\!] \quad (48)$$

$$\mathbf{F}^H = \frac{1}{2} \hat{\mathbf{n}} \times [\![\mathbf{H}]\!] \quad (49)$$

for the central flux, and

$$\mathbf{F}^E = \frac{1}{Y^+ + Y^-} (Y^+ \hat{\mathbf{n}} \times [\![\mathbf{E}]\!] + \hat{\mathbf{n}} \times \hat{\mathbf{n}} \times [\![\mathbf{H}]\!]) \quad (50)$$

$$\mathbf{F}^H = \frac{1}{Z^+ + Z^-} (Z^+ \hat{\mathbf{n}} \times [\![\mathbf{H}]\!] - \hat{\mathbf{n}} \times \hat{\mathbf{n}} \times [\![\mathbf{E}]\!]) \quad (51)$$

for the upwind flux, while

$$[M^e]_{ij} = \int_{V_e} l_i l_j dV \quad (52)$$

$$[S_w^e]_{ij} = \int_{V_e} l_i \frac{\partial l_j}{\partial w} dV \quad (53)$$

$$[M_f^e]_{ij} = \int_{\partial V_e} l_i l_j dS \quad (54)$$

are mass, stiffness, and facial mass matrices defined in each tetrahedron element  $V_e$  and its surface  $\partial V_e$ , respectively.

To solve the above equations, the momentum transfer equation needs to be solved simultaneously. Since it is valid in a point-wise manner, no numerical flux is needed. Using the similar discretization method, the momentum transfer equation can be converted into a set of matrix equations ( $w = x, y, \text{ or } z$ )

$$\dot{J}_{cw} = -v_m J_{cw} + \frac{e^2 n}{m} (E_w + E_w^{\text{inc}}) \quad (55)$$

When Maxwell's equations and the momentum transfer equation are solved together, the current values of the physical quantities  $\mathbf{E}$ ,  $\mathbf{H}$ , and  $\mathbf{J}_c$  are substituted into the RHS of the above matrix equations to obtain the time derivative of themselves, which are then used to obtain their updated values at the next time step using an explicit time integration scheme.

### 3.3.1.2 Local DGTD for the Parabolic PDE – Electron Diffusion Equation

The diffusion equation has a very different mathematical property from Maxwell's equations because of the different orders in the spatial derivative. For the diffusion equation, if a similar method as described in the preceding section is adopted, a convergent but inconsistent numerical solution will be produced [34]. Here, the term “convergent” is used to refer to the fact that when fixing the polynomial order but increasing the spatial discretization density ( $h$ -refinement), the numerical result will converge to some certain solution; the term “inconsistent” is used to refer to the fact that the convergent solutions for different polynomial orders ( $p$ -refinement) are different. As a result, a different DG scheme needs to be used to obtain a numerical solution that is both convergent and consistent.

In this work, the local discontinuous Galerkin (LDG) method in time domain [17] is adopted, with the basic idea and formulations described below.

Consider the diffusion equation

$$\dot{u} - \nabla \cdot (D \nabla u) = f \quad (\mathbf{r}, t) \in \Omega \times [0, \infty) \quad (56)$$

subject to the following boundary and initial conditions

$$u(\mathbf{r}, t) = g_D \quad \mathbf{r} \in \Gamma_D \quad (57)$$

$$\hat{\mathbf{n}} \cdot D \nabla u(\mathbf{r}, t) = g_N \quad \mathbf{r} \in \Gamma_N \quad (58)$$

$$au + \hat{\mathbf{n}} \cdot D \nabla u(\mathbf{r}, t) = g_R \quad \mathbf{r} \in \Gamma_R \quad (59)$$

$$u(\mathbf{r}, 0) = u_0 \quad \mathbf{r} \in \Omega \quad (60)$$

where  $\Omega$  denotes the three dimensional solution domain,  $\Gamma_D$ ,  $\Gamma_N$ , and  $\Gamma_R$  denote the Dirichlet, Neumann, and Robin boundaries, respectively. To solve it with DG method, we define an auxiliary variable  $\mathbf{q} = \nabla u$  and rewrite the above equations as two coupled equations with only first order derivatives in space

$$\mathbf{q} - \nabla u = 0 \quad (\mathbf{r}, t) \in \Omega \times [0, \infty) \quad (61)$$

$$\dot{u} - \nabla \cdot (D\mathbf{q}) = f \quad (\mathbf{r}, t) \in \Omega \times [0, \infty) \quad (62)$$

$$u(\mathbf{r}, t) = g_D \quad \mathbf{r} \in \Gamma_D \quad (63)$$

$$\hat{\mathbf{n}} \cdot D\mathbf{q}(\mathbf{r}, t) = g_N \quad \mathbf{r} \in \Gamma_N \quad (64)$$

$$au + \hat{\mathbf{n}} \cdot D\mathbf{q}(\mathbf{r}, t) = g_R \quad \mathbf{r} \in \Gamma_R \quad (65)$$

$$u(\mathbf{r}, 0) = u_0 \quad \mathbf{r} \in \Omega. \quad (66)$$

Testing the above equations with Lagrange polynomials  $l_i$  and  $\mathbf{l}_i = \hat{\mathbf{w}} l_i$  ( $\hat{\mathbf{w}} = \hat{\mathbf{x}}, \hat{\mathbf{y}}$ , or  $\hat{\mathbf{z}}$ ) on each tetrahedron element  $V_e$ , and applying the divergence theorem twice yield the strong form

$$\int_{V_e} \mathbf{l}_i \cdot \mathbf{q} \, dV = \int_{V_e} \mathbf{l}_i \cdot \nabla u \, dV - \oint_{\partial V_e} \mathbf{l}_i \cdot \hat{\mathbf{n}} (u - u^*) \, dS \quad (67)$$

$$\int_{V_e} l_i \dot{u} \, dV = \int_{V_e} l_i \nabla \cdot (D\mathbf{q}) \, dV - \oint_{\partial V_e} l_i \hat{\mathbf{n}} \cdot [D\mathbf{q} - (D\mathbf{q})^*] \, dS + \int_{V_e} l_i f \, dV. \quad (68)$$

In the above strong form,  $u^*$  and  $(D\mathbf{q})^*$  are the numerical fluxes defined on the boundary faces of each tetrahedron element. Two choices of these numerical fluxes are commonly applied. They are given below using the average  $\{\cdot\}$  and jump  $[\![\cdot]\!]$  functions defined in the preceding section.

- Central Flux

$$u^* = \{u\}, \quad (D\mathbf{q})^* = \{D\mathbf{q}\} \quad (69)$$

- LDG Flux

$$u^* = \{u\} + \boldsymbol{\gamma}^e \cdot \hat{\mathbf{n}} [\![u]\!] \quad (70)$$

$$(D\mathbf{q})^* = \{D\mathbf{q}\} + \boldsymbol{\beta}^e \hat{\mathbf{n}} \cdot [\![D\mathbf{q}]\!] - \eta^e \hat{\mathbf{n}} [\![u]\!] \quad (71)$$

where

$$\hat{\mathbf{n}} \cdot \boldsymbol{\beta}^e = \frac{1}{2} \text{sign}(\hat{\mathbf{n}} \cdot \hat{\mathbf{r}}), \quad \hat{\mathbf{n}} \cdot \boldsymbol{\gamma}^e = -\frac{1}{2} \text{sign}(\hat{\mathbf{n}} \cdot \hat{\mathbf{r}}) \quad (72)$$

with  $\hat{\mathbf{r}}$  being a given constant vector to mimic the wind direction, and  $\eta^e > 0$  to serve as a penalty factor.

Expanding  $u$  and  $\mathbf{q}$  in terms of  $p$ th order Lagrange polynomial basis functions

$$u = \sum_{j=1}^{N_p} l_j u_j, \quad \mathbf{q} = \sum_{j=1}^{N_p} l_j (\hat{\mathbf{x}} q_{xj} + \hat{\mathbf{y}} q_{yj} + \hat{\mathbf{z}} q_{zj}) \quad (73)$$

and substituting them into the strong form to obtain the matrix form representation of the diffusion equation ( $w = x, y$ , or  $z$ )

$$M^e q_w = S_w^e u - M_f^e [n_w(u - u^*)] \quad (74)$$

$$M^e \dot{u} = \sum_w S_w^e D q_w - M_f^e \sum_w n_w [D q_w - (D q_w)^*] + M^e f. \quad (75)$$

To solve the diffusion equation, the auxiliary variable  $\mathbf{q}$  is first calculated using the information of  $u$ , and the time derivative  $\dot{u}$  is then obtained using the values of both  $u$  and  $\mathbf{q}$ . The value of  $u$  at the next time step can be obtained with a time integration scheme which will be discussed later.

### 3.3.2 Higher-Order Spatial Discretization

After the discussion on the formulation for different equations, the high order basis functions themselves need to be introduced. In this section, the commonly used high order basis functions, the high order hierarchical basis functions and the high order interpolatory basis functions, are introduced, and both basis functions are used in the development of our coupled DGTD method. Since tetrahedron elements are used in the geometric discretization of the solution domain, basis functions that are defined on tetrahedrons will be introduced. Nevertheless, those defined on different types of elements can also be defined in a similar fashion.

#### 3.3.2.1 Definition of Basis Functions: Modal Basis and Nodal Basis

Unlike that of the high-order vector basis functions widely used by the computational electromagnetics community, the definition of the high-order scalar basis functions is a bit different. The high-order hierarchical basis functions, which are more commonly known as the *modal basis*, are a set of orthonormal polynomials defined on the simplex, which is a tetrahedron in 3D. Specifically, the following orthonormal polynomial of order  $p \geq i + j + k \geq 0$  are defined using the well-known Jacobi polynomials

$$\psi_{ijk}(r, s, t) = \sqrt{8} P_i^{0,0}(a) P_j^{2i+1,0}(b) (1-b)^j P_k^{2i+2j+2,0}(c) (1-c)^{i+j} \quad (76)$$

where  $a = -2\frac{1+r}{s+t} - 1$ ,  $b = 2\frac{1+s}{1-t} - 1$ , and  $c = t$ , with the 3D simplex defined by  $r, s, t \geq -1$ ,  $r + s + t \leq -1$ . The Jacobi polynomials are given by

$$P_n^{\alpha, \beta}(z) = \frac{(-1)^n}{2^n n!} (1-z)^{-\alpha} (1+z)^{-\beta} \frac{d^n}{dz^n} \{(1-z)^\alpha (1+z)^\beta (1-z^2)^n\}. \quad (77)$$

When  $\alpha = \beta = 0$ , the Jacobi polynomial reduces to the Legendre polynomials

$$P_n(z) = \frac{1}{2^n n!} \frac{d^n}{dz^n} \{(z^2 - 1)^n\}. \quad (78)$$

Note that the modal basis are hierarchical in nature, meaning that a set of higher order modal basis contains all of the lower order modal basis (similar to the Fourier basis).

The physical quantity can therefore be expanded in terms of the modal basis as (here the subscript  $i, j, k$  are lumped into  $n$  for simplicity)

$$u(\mathbf{x}, t) = \sum_{n=1}^{N_p} \hat{u}_n(t) \psi_n(\mathbf{x}). \quad (79)$$

The definition of high-order interpolatory basis functions has multiple choices. For example, one can use monomials

$$\zeta^i \eta^j \xi^k, \quad i, j, k \geq 0, i + j + k \leq p \quad (80)$$

or polynomials as the basis functions. Here the widely used Lagrange polynomials are used as the high-order interpolatory basis functions. One unique property of the Lagrange polynomial is that its value is one only at one interpolating node (which is known as its definition node), but zeroes on all other  $N_p - 1$  interpolating nodes. It is for this reason that the Lagrange basis functions are better known as *nodal basis*, as opposed to the modal basis introduced earlier. This property has two pleasing consequences. One is that the expansion coefficient of each Lagrange basis function stands for the value of the physical quantity at the definition node of the basis function. The other is that when using the Lobatto nodes to define the Lagrange basis functions (will be introduced in the next section), the value of a Lagrange basis function defined in a  $d$ -dimensional simplex is purely zero on any of its lower  $d'$ -dimensional simplex subset ( $0 \leq d' < d$ ), if the definition node of the basis function is not in that  $d'$ -dimensional simplex. For example, for the Lagrange basis defined inside the volume of a tetrahedron, its value is purely zero on all the four faces, six edges, and four vertices of the tetrahedron. This property is especially useful when implementing the DG method, because when trying to collect the values for the numerical flux, all matters are the DoFs that are defined on the common triangle of two neighboring tetrahedrons, and all other DoFs have zero contribution.

The difficulty of applying the Lagrange basis functions in a high order polynomial expansion is that there are no general explicit expressions for high order Lagrange polynomials. In a

calculation that involves the Lagrange polynomial, what one can do is to relate the Lagrange basis function (nodal basis) to the orthonormal basis function (modal basis) as

$$u(\boldsymbol{x}, t) = \sum_{i=1}^{N_p} u(\boldsymbol{x}_i, t) l_i(\boldsymbol{x}) = \sum_{n=1}^{N_p} \hat{u}_n(t) \psi_n(\boldsymbol{x}) \quad (81)$$

where  $l_i$  denotes the 3D Lagrange polynomials defined on the interpolating node  $\boldsymbol{x}_i$ . Matching the values of  $u$  at all the interpolating nodes  $\boldsymbol{x}_i$  ( $i = 1, \dots, N_p$ ) yields

$$\mathcal{V}\hat{\boldsymbol{u}} = \boldsymbol{u} \quad (82)$$

where  $\mathcal{V}_{nm} = \psi_m(\boldsymbol{x}_n)$  is the generalized Vandermonde matrix,  $\hat{\boldsymbol{u}} = \{\hat{u}_1, \dots, \hat{u}_{N_p}\}^T$ , and  $\boldsymbol{u} = \{u_1, \dots, u_{N_p}\}^T$ . The Lagrange polynomials can thus be expressed as

$$l_n(\boldsymbol{x}) = \sum_{m=1}^{N_p} (\mathcal{V}^{-1})_{mn} \psi_m(\boldsymbol{x}), \text{ or } \boldsymbol{l} = \mathcal{V}^{-T} \boldsymbol{\psi} \quad (83)$$

and can be used to calculate the elemental matrices which will be discussed in a following section.

### 3.3.2.2 Choice of Interpolating Nodes

One very important aspect of applying the Lagrange basis functions is how to choose the interpolating nodes. If a set of equi-spaced nodes is used to define the Lagrange basis functions, the famous Runge phenomenon will lead to a highly oscillating function value when very high order polynomials are used. The oscillation becomes even worse near the boundary of the definition domain of the polynomial, which would completely ruin the DG method where the numerical flux plays a central role of the algorithm. To remove the Runge phenomenon, a set of nonuniformly spaced nodes is usually used to define the Lagrange polynomial, which is often the root set of certain polynomials defined in the same simplex. Examples of such polynomials include the Legendre polynomial, the Chebyshev polynomials of the first or the second kind, and the Lobatto polynomial. For the application of DG method, the Lobatto nodes are especially attractive, since the node set includes those on the boundary of a simplex, which becomes handy when calculating the numerical flux. Unfortunately, the Lobatto nodes in 3D simplex are not well-defined. There are several approaches of getting the Lobatto nodes. For example, to minimize the Lebesgue constant, this is a quantity that measures the interpolation quality of a given polynomial, or to maximizing the magnitude of the determinant of the Vandermonde matrix using either constraint optimization method or Monte Carlo method. In this work, a set of optimized Lobatto nodes in 3D simplex is used, as shown in Figure 2 adopted from [19]. The optimized set of nodes produces a small Lebesgue constant when compared to other node sets available in the literature, and reduces to 1D Gauss-Lobatto-Legendre (GLL) node set on the edges of the tetrahedron.

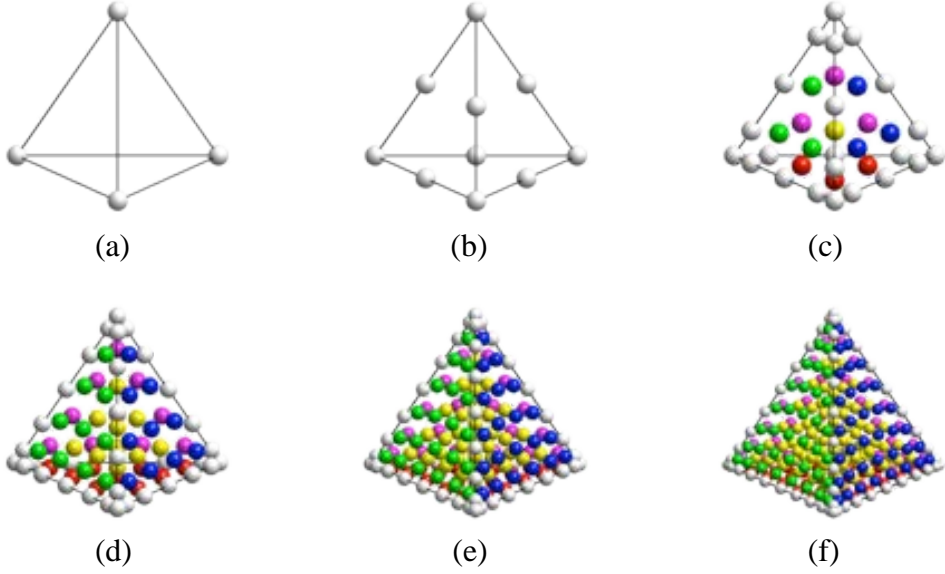


**Figure 2. Optimized Interpolating Nodes in Tetrahedron [19].** (a)  $p = 1$ , (b)  $p = 2$ , (c)  $p = 4$ , (d)  $p = 6$ , (e)  $p = 8$ , and (f)  $p = 10$

Multiple advantages of choosing an optimal set of interpolating nodes can be achieved. The first one is that it results in a smaller Lebesgue constant, and therefore, a better interpolation quality. Second, it also reduces the spectral radius of the facial matrix  $M^{-1}T_f$ , where  $T_f$  is the same as  $M_f$ , with its number of row expanded to  $N_p$  to allow the matrix-matrix product with  $M^{-1}$ . Since the spectral radius  $\rho(M^{-1}T_f)$  determines the time step size required to maintain stability, a smaller spectral radius results in a larger time step size, and consequently, a more efficient algorithm. Shown in Figure 3 is the comparison made between the widely-used hierarchical vector basis functions and the orthonormal basis functions used in this work. From Figure 3(a), the spectral radius of the orthonormal basis functions is smaller than that of the vector basis, and hence results a larger step size as can be seen in Figure 3(b).

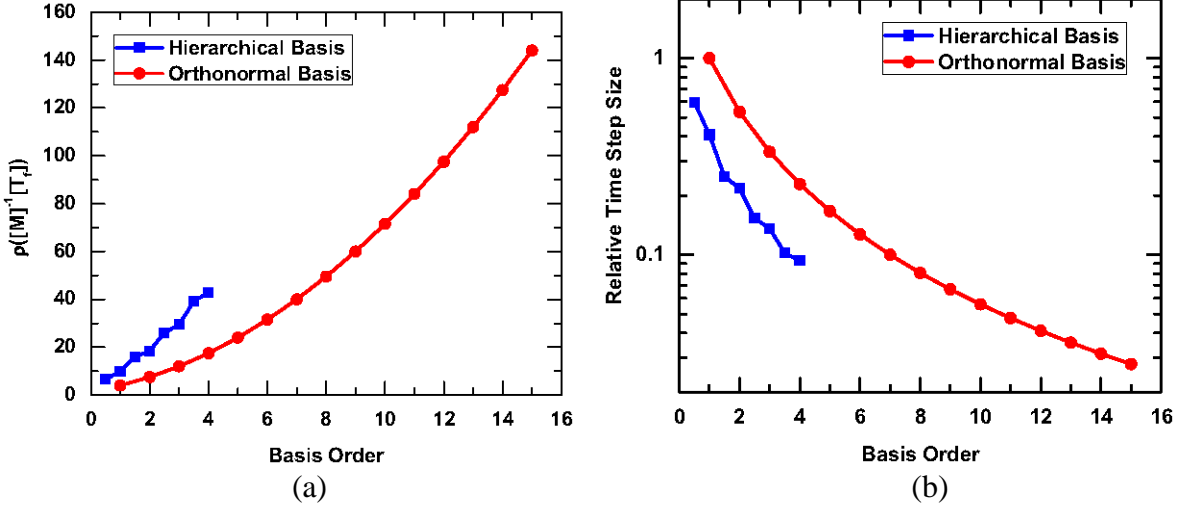


**Figure 3. (a) Spectral Radius of the Facial Matrix Versus Polynomial Basis Order; (b) Time Step Size Required to Maintain Stability Versus Polynomial Basis Order. The Time Step Sizes Are Normalized Against That of the First-Order Orthonormal Basis Function**

### 3.3.2.3 Elemental Matrices in the DG Method

After the high-order basis functions and the associated definition nodes are obtained, the elemental matrices in the DG method can be explicitly expressed. In this section, the calculation of the mass, stiffness, and facial mass matrices are discussed.

We start from the calculation of the mass matrix. Using the relation  $\mathbf{l} = \mathcal{V}^{-T} \boldsymbol{\psi}$ , the mass matrix can be expressed as

$$M^e = J^e \int_I \mathbf{l} \mathbf{l}^T dV = J^e \mathcal{V}^{-T} \int_I \boldsymbol{\psi} \boldsymbol{\psi}^T dV \mathcal{V}^{-1} \quad (84)$$

where  $I$  is the reference simplex in 3D, and  $J^e$  is the Jacobian matrix mapping from the reference simplex to the real tetrahedron, and is reduced to a single scalar if the geometric discretization is linear (1st order tetrahedron). Since the modal basis are orthonormal, the mass matrix can be written in an explicit form as

$$M^e = J^e (\mathcal{V} \mathcal{V}^T)^{-1} = J^e M. \quad (85)$$

Note that in the explicit form of the mass matrix, no numerical quadrature is required. The facial mass matrix can be obtained in a similar manner; the only difference is that everything in the explicit expression reduces from 3D to 2D as

$$M_f^e = J_f^e (\mathcal{V}_f \mathcal{V}_f^T)^{-1} = J_f^e M_f. \quad (86)$$

The stiffness matrix involves the partial derivative with respect to  $x$ ,  $y$ , or  $z$ . Here we take  $S_x^e$  for example to illustrate its calculation.

$$\begin{aligned} [S_x^e]_{ij} &= \int_{V_e} l_i \frac{\partial l_j}{\partial x} dV = \int_{V_e} l_i \left( \frac{\partial l_j}{\partial r} \frac{\partial r}{\partial x} + \frac{\partial l_j}{\partial s} \frac{\partial s}{\partial x} + \frac{\partial l_j}{\partial t} \frac{\partial t}{\partial x} \right) dV \\ &= r_x \int_I l_i \frac{\partial l_j}{\partial r} dV + s_x \int_I l_i \frac{\partial l_j}{\partial s} dV + t_x \int_I l_i \frac{\partial l_j}{\partial t} dV \end{aligned} \quad (87)$$

In the above derivation, the derivatives  $r_x$ ,  $s_x$ , and  $t_x$  are constants if linear tetrahedron elements are used, and the integration terms can be further written as

$$\int_I l_i \frac{\partial l_j}{\partial r} dV = \int_I l_i \left( \sum_{n=1}^{N_p} \frac{\partial l_j}{\partial r} \Big|_{r_n} l_n \right) dV = \sum_{n=1}^{N_p} \left( \int_I l_i l_n dV \frac{\partial l_j}{\partial r} \Big|_{r_n} \right) = \sum_{n=1}^{N_p} M_{in} D_{r,nj} \quad (88)$$

where the interpolation of  $\frac{\partial l_j}{\partial r}$  using Lagrange polynomials is applied, and  $D_{r,nj}$  is the differential matrix with respect to the variable  $r$

$$D_{r,nj} = \frac{\partial l_j}{\partial r} \Big|_{r_n} \quad (89)$$

which can also be expressed analytically using the relation between the Lagrange and the orthonormal basis functions. Details will not be given here. The stiffness matrix can finally be expressed as

$$S_x^e = M (r_x D_r + s_x D_s + t_x D_t) \quad (90)$$

and  $S_y^e$  and  $S_z^e$  can be expressed similarly.

### 3.3.3 Higher Order Temporal Discretization

After the system equations are discretized with high order basis functions in space, a set of ODEs can be obtained and formally written as

$$\dot{u} = F(t, u), \quad u(t_0) = u_0. \quad (91)$$

The system of ODEs can be solved using the well-known explicit high order Runge-Kutta methods [35], for instance, the classic fourth order Runge-Kutta method, to achieve the high order accuracy in time. However, the traditional Runge-Kutta methods are in general not strong-stability preserving (SSP), and the SSP coefficient (which is the ratio between the maximum time step size for a given time integrator and that for the forward Euler's method)  $\mathcal{C} \approx 1$ .

In this work we employ the SSP Runge-Kutta (SSPRK) method [36], which is also known as the total variation diminishing (TVD) Runge-Kutta Method [37][38] in the past. The strong-stability

preserving property means that if the embedded first order Euler's method is stable, the high order SSPRK method is also stable, which diminishes the total variation in the solution. In the meantime, the SSP coefficient can be made larger to allow a larger time step size. For example, the low-storage four-stage third-order SSPRK is given by

$$q_1 = u^n \quad (92)$$

$$q_2 = q_1 + \frac{h}{2} F(q_1) \quad (93)$$

$$q_2 = q_2 + \frac{h}{2} F(q_2) \quad (94)$$

$$q_2 = \frac{2}{3} q_1 + \frac{1}{3} \left[ q_2 + \frac{h}{2} F(q_2) \right] \quad (95)$$

$$u^{n+1} = q_2 + \frac{h}{2} F(q_2) \quad (96)$$

and the SSP coefficient  $\mathcal{C} = 2$ . In this work, a low-storage ten-stage fourth-order SSPRK is employed because of its large SSP coefficient  $\mathcal{C} = 6$  which makes it more efficient than other SSPRK methods.

Despite its attractive properties, the SSPRK methods have their own issue that they are originally designed for PDE with a constant coefficient operator  $F(u)$ , which means on the RHS of the equation, no time variable can be involved. When looking back to the coupled system equations we are dealing with, it is realized that the SSPRK methods can be applied directly to Maxwell's equations and the electron diffusion equation. However, since the incident field directly involves the time variable in its definition, SSPRK cannot be applied in a straightforward way. In this work, this issue is resolved by defining auxiliary variables as detailed next.

Since  $\mathbf{E}^{\text{inc}} = \mathbf{E}_0 \sin[\omega(t - \tau)] = \mathbf{E}_0 [\cos(\omega\tau) \sin(\omega t) - \sin(\omega\tau) \cos(\omega t)]$ , where  $\tau$  is the time delay associated with each spatial point  $\mathbf{r}$  with respect to a reference point  $\mathbf{r}_0$ ,  $\tau = (\mathbf{r} - \mathbf{r}_0) \cdot \hat{\mathbf{k}}^{\text{inc}}/c$ , by defining two auxiliary variables  $f_1 = \sin(\omega t)$  and  $f_2 = \cos(\omega t)$ , a new system with a constant coefficient operator is obtained as

$$\dot{\mathbf{H}} = -\frac{1}{\mu} \nabla \times \mathbf{E} \quad (97)$$

$$\dot{\mathbf{E}} = \frac{1}{\epsilon} (\nabla \times \mathbf{H} - \mathbf{J}_c) \quad (98)$$

$$\dot{\mathbf{J}}_c = -v_m \mathbf{J}_c + \frac{e^2 n}{m} \mathbf{E} + \frac{e^2 n}{m} \mathbf{E}_0 [\cos(\omega\tau) f_1 - \sin(\omega\tau) f_2] \quad (99)$$

$$\dot{f}_1 = \omega f_2 \quad (100)$$

$$\dot{f}_2 = -\omega f_1. \quad (101)$$

Therefore, the SSPRK method can be applied and the high-order accuracy in both time and space is achieved with a relaxed stability condition.

## 3.4 Computational Acceleration Techniques

As pointed out in the preceding section, the physical problem we are dealing here is a multiscale problem, which requires an extremely intensive computation to complete the whole simulation. In order to make the method practical, two very effective acceleration techniques have been developed in this work. One uses the software-based (algorithm-based) acceleration technique; the other uses the hardware-based acceleration technique.

### 3.4.1 Dynamic $p$ -Adaption

To resolve the fast varying physical quantity, one approach is to use higher-order basis functions, which is known as the  $p$ -refinement. However, the application of a uniformly high-order basis functions will result in a very large number of DoFs in the system, which makes the simulation prohibitively long. In the simulation of the time domain evolution of the plasma, the plasma front, where the largest density gradient is located, needs the highest spatial resolution, and is moving with time, while the rest of the plasma region is relatively smooth and slowly varying. To take the advantage of the higher-order basis function and control the overall computational cost, a flexible dynamic  $p$ -adaption algorithm is developed in this work. Instead of using a uniform polynomial order throughout the entire solution domain, the algorithm first identifies regions that need higher spatial resolution, (and therefore, higher polynomial order) versus those do not need such high order spatial resolution. Since the plasma is evolving and propagating in space and time, this identification process is made dynamic such that the order of a given tetrahedron element is adjusted according to the specific need.

The important point in the dynamic adjustment is to find a good measuring quantity to determine the polynomial order. Take the electron density for example, since the high order polynomial is employed to resolve its spatial variation, how fast it actually varies in space would be a good indicator of the polynomial order needed. As a result, the magnitude of the gradient of the electron density turns out to be the intended indicator for the dynamic  $p$ -adaption algorithm. Shown in Figure 4 is the contour plot of the electron plasma density and its gradient, which reveals the fact that around the plasma front, the electron density decreases fastest and therefore need a higher order polynomial for it to be resolved.

In addition to determining the polynomial order based on the density gradient, other constraints can also be set. For example, one can require that the order difference between two adjacent tetrahedrons be smaller than some preset value to avoid sudden change of spatial resolution and the resulting numerical instability.

The process of dynamic  $p$ -adaption is summarized as following steps.

1. Set initial conditions;
2. Dynamic  $p$ -adaption: change basis orders adaptively based on  $\|\nabla n\|$  and other constraints;
3. Elevate elemental DoFs:  $n$ ,  $\mathbf{E}$ ,  $\mathbf{H}$ , and  $\mathbf{J}_c$ ;
4. Change facial connectivity array;

5. Solve the system equations: elevate facial DoFs at every stage of the SSPRK method to calculate numerical fluxes;
6. Go to step 2, march on in time until the problem is solved.

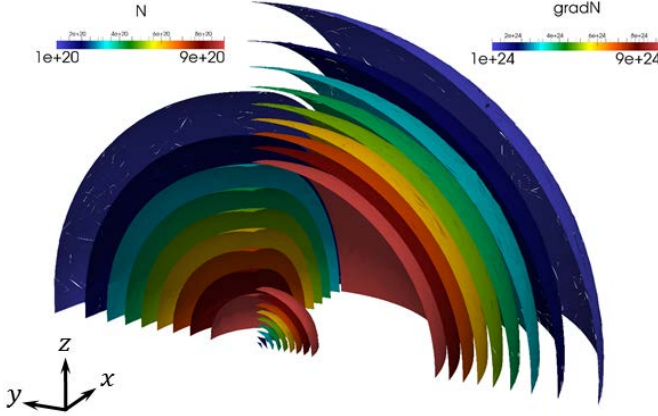


**Figure 4. Contour Plot of the Electron Density (Left Half) and it's Gradient (Right Half)**

### 3.4.2 GPU Acceleration

The DGTD method is in fact an element level domain decomposition method, which decomposes the entire solution domain into discretization elements, and solves the governing equations within each of the elements. With the aid of the explicit Runge-Kutta method, all the information needed from the neighboring elements is readily obtained from the previous time steps. As a result, the DGTD method can be parallelized with a very high efficiency. In this work, the coupled DGTD algorithm is parallelized using graphics processing units (GPUs) using NVIDIA’s CUDA (compute unified device architecture) parallel programming models [39].

#### 3.4.2.1 Single GPU Acceleration

A big advantage for the DGTD method to be accelerated by GPU is that it does not require the storage of elemental matrices. As described in Section IV-2.3, the matrices that need to be stored are those defined on the reference simplex  $M$ ,  $M_f$ ,  $D_r$ ,  $D_s$ , and  $D_t$ . The element-related variables are only several constants for each element, which include  $J^e$ ,  $J_f^e$ ,  $r_{x,y,z}$ ,  $s_{x,y,z}$ , and  $t_{x,y,z}$ . This nice property of the DGTD method (for linear elements) makes it extremely storage-efficient. As a result, even a very large problem can be solved on a single GPU card where the memory is limited. The implementation of the nodal DGTD method on GPU is similar to those reported in [40][41], and will not be detailed here. When the GPU is enabled, the computational speed-up is about 10 times compared to the OpenMP-parallelized CPU code running on eight CPU cores.

### 3.4.2.2 GPU Acceleration of the DGTD Algorithm with $p$ -Adaption

Since the dynamic  $p$ -adaption algorithm is developed in CPU-based code, it is desired to extend this capability to GPUs for a better efficiency. However, the extension from a GPU code with uniform polynomial order to dynamic orders is quite challenging, because the flexibility of the  $p$ -adapted code would prevent the GPU implementation from having a high parallel efficiency. In this work, the GPU algorithm with dynamic  $p$ -adaption technique is carefully designed to maximize its parallel efficiency. The matrices for all possible polynomial orders that are defined on the reference simplex are pre-stored in the GPU global memory to allow the potential matrix-vector products for the corresponding order. In addition, the elevation matrices that elevate elemental DoFs between different orders are also pre-stored in the GPU global memory. At a specific time step in the time-stepping process, the entire solution domain is first scanned, and the DoFs in different tetrahedrons are elevated (either increased or decreased) to the correct polynomial order whenever and wherever needed. The numerical fluxes on the surfaces that interface with tetrahedrons of different polynomial orders are then calculated to permit the correct information exchange between neighboring tetrahedrons. The tetrahedrons with the same polynomial order are then aligned in the same streaming array and processed together since they are all multiplied by the same matrices, to obtain an optimized speed-up. The dynamic  $p$ -adapted GPU algorithm can eventually achieve about eight-time speed-up compared with the dynamic  $p$ -adapted CPU algorithm running in parallel on eight CPU cores.

## 4.0 RESULTS AND DISCUSSION

Numerical results are given in this section to demonstrate the accuracy of the DGTD method and model several physical phenomena related to the high-power microwave breakdown and the plasma formation and evolution. The extremely high gradient of the electron density distribution is resolved by using either a dense geometrical discretization or a set of higher order basis functions.

### 4.1 Validation of the LDG Method for the Diffusion Equation

The first example given here is the solution of the diffusion equation using the LDG method for the validation purpose. Consider the following density diffusion problem with a diffusion coefficient  $D = 1$

$$\dot{u} - \nabla \cdot (D \nabla u) = 0 \quad (\mathbf{r}, t) \in \Omega \times [0, \infty) \quad (102)$$

$$u(\mathbf{r}, t) = 0 \quad \mathbf{r} \in \Gamma_D \quad (103)$$

$$u(\mathbf{r}, 0) = u_0 \quad \mathbf{r} \in \Omega \quad (104)$$

defined in a spherical solution domain  $\Omega$  where  $r \in [0, a]$  ( $a = 2$  mm). The initial condition of the density distribution is a Gaussian function with a standard deviation  $\sigma = 0.4$  mm

$$u_0 = e^{-\frac{r^2}{2\sigma^2}}. \quad (105)$$

This problem has an analytical solution given by

$$u(\mathbf{r}, t) = \sum_{n=1}^{\infty} c_n j_0(\beta_n r) e^{-\beta_n^2 t} \quad (106)$$

where  $j_0$  is the zeroth order spherical Bessel function of the first kind,  $\beta_n = \frac{n\pi}{a}$ , and  $c_n$  can be found by matching the initial condition.

This problem is solved numerically using the LDG method in time for a total of  $N_t = 13150$  time steps with a time step size  $\Delta t = 20$  ps. The final result along the center line of the solution domain at  $t = 263$  ns is compared with the analytical solution and is shown in Figure 5, from which excellent agreement can be observed. Figure 6 shows the contour plot of the equal-density surfaces of the electron density distribution at the final time step. It can be seen from this figure that even after time stepping for over 13 thousand steps, the equal-density surfaces of the density distribution given by the numerical solution is still very smooth, which demonstrates the high accuracy of the LDG method employed in this project.

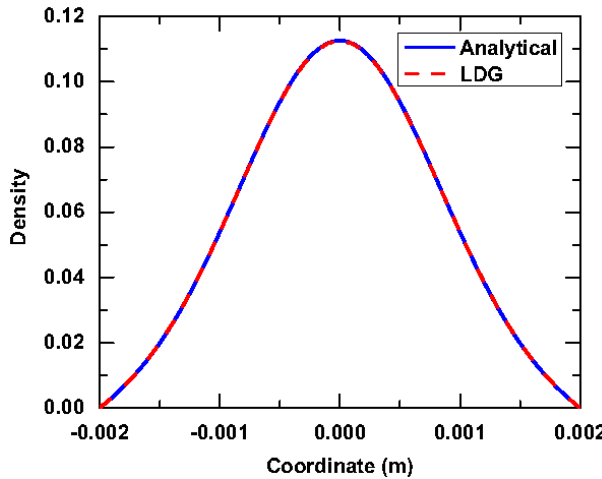


**Figure 5. Comparison between the Numerical and the Analytical Solutions of the Diffusion Equation**



**Figure 6. Contour Plot of the Density Distribution at the Final Time Step**

## 4.2 Modeling of Plasma Shielding of the Electromagnetic Wave

In this example, the air breakdown under the high-power microwave operation and the formation and evolution of the plasma is simulated. This problem is adopted from [33] and was originally simulated with FDTD and FVTD (finite volume time domain) methods in two dimensions. In this work, this example is reproduced using the DGTD method in three dimensions.

### 4.2.1 Physics Involved

During the high-power microwave operation, the electric field with a high power density will ionize neutral gas and produce electrons and positive ions. If the power density of the electric field is high enough, such an ionization process will continue, which results in an exponential increase of the electron density known as breakdown. However, this process will not go on forever. According to the basic plasma physics, when the plasma density increases to a point that the corresponding plasma frequency becomes greater than the incident frequency, the electrons in the plasma bulk can oscillate fast enough such that the secondary fields radiated from the electron oscillation cancels the primary (incident) fields. Macroscopically, the plasma bulk is acting like a piece of electromagnetic shield which prevents the electromagnetic wave from propagating through. This leads to a decrease of the total electric field intensity in the plasma bulk which lowers the ionization rate. As a result, the electron density will get saturated at a certain level and the entire system will run into a steady state.

### 4.2.2 Numerical Settings

As shown in Figure 7, the solution domain considered in this example is a parallel plate waveguide with a metallic wall placed in between of the two parallel plates, which forms a rectangular aperture (denoted in red in the figure). The solution domain is truncated from the left and the right using the ABC. Different from the 2D problem considered in [33], in this work a 3D problem is solved by setting a thickness to the structure (the dimension not shown in Figure 7) and placing the PMC boundary conditions on both sides in the thickness direction to reproduce the 2D phenomenon in 3D. A set of 25-GHz, 2.0-MV/m, vertically polarized plane

wave with a tapered sinusoidal temporal profile is launched from the left boundary and propagates toward the right direction (the  $z$  direction).

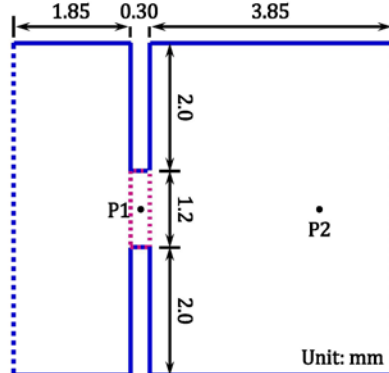


**Figure 7. Illustration of the Solution Domain of the Microwave Breakdown Problem in a Metallic Aperture**

Two cases are considered and compared in this example. One is the vacuum case where the entire structure is assumed to be filled with vacuum, and therefore, the metallic wall is simply reflecting a portion of the incident wave and enhancing the fields in the aperture area. The other is the air case where the 100-torr low pressure air is assumed to be confined in the aperture area, with the rest of the domain filled with vacuum. When the plane wave is incident upon the air region, it is enhanced by the metallic wall and triggers the air breakdown. In the numerical simulation, four boundaries of the air aperture are set as homogeneous Dirichlet boundaries for the electron density, and the other two boundaries in the thickness ( $x$ ) direction are set as homogeneous Neumann boundaries. To satisfy the Dirichlet boundary condition, the initial spatial profile of the electron density is set to be sinusoidal in both the vertical ( $y$ ) and the horizontal ( $z$ ) directions, which reaches its maximum value of  $10^{15}/\text{m}^3$  at the center of the aperture. In the  $x$  direction, the electron density distribution is uniform.

In both cases, the electric field is recorded at two observation points P1 ( $x = y = 0.0$  mm,  $z = 0.0$  mm) and P2 ( $x = y = 0.0$  mm,  $z = 2.81$  mm) shown in Figure 7. In the air case, the electron density  $n$  and the effective field  $E_{\text{eff}}$  in the air region are also recorded to demonstrate the spatial and temporal evolution of the plasma.

#### 4.2.3 Numerical Results and Analysis

Shown in Figure 8 is the temporal profile of the electric fields recorded at P1 and P2 in both the vacuum and the air cases. Different behaviors can be observed in the two cases. In the vacuum case, the electric field intensity at both observation points follows the tapered sinusoidal profile of the incident wave, with the field at P1 point enhanced by the narrow aperture, and that at P2 point weakened comparing with the magnitude of the incident wave (2 MV/m) due to the partial reflection of the incident wave by the metallic wall. In the air case, however, the electric field intensity recorded at both observation points increases in the early time, but decreases suddenly at P1 point and gradually at P2 point, and becomes stabilized at much lower values after 0.5 ns.

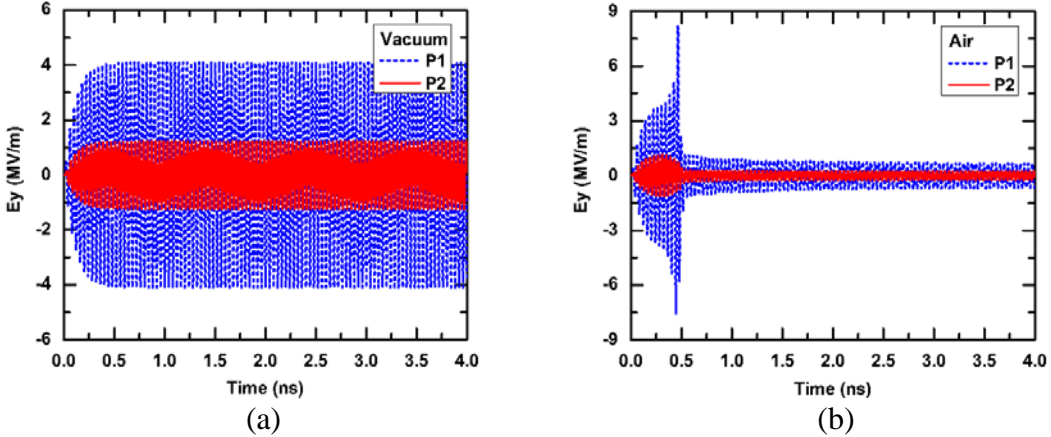


**Figure 8. Temporal Response of the Electric Fields Recorded at P1 and P2 in (a) the Vacuum and (b) the Air Cases**

The electric fields recorded in both cases at P2 point are compared in Figure 9(a), from which it is clear that the electric field observed in the air case agrees well with that in the vacuum case up to 0.35 ns. After that, the electric field in the air case starts to get shielded and its magnitude decreases and gets stabilized after 0.5 ns. From the electron density recorded at P1 point shown in Figure 9(b), it can be seen that initially the electron density increases exponentially from its initial value of  $10^{15}/\text{m}^3$  to over  $10^{21}/\text{m}^3$  within the first 0.5 ns, and gets saturated afterwards.

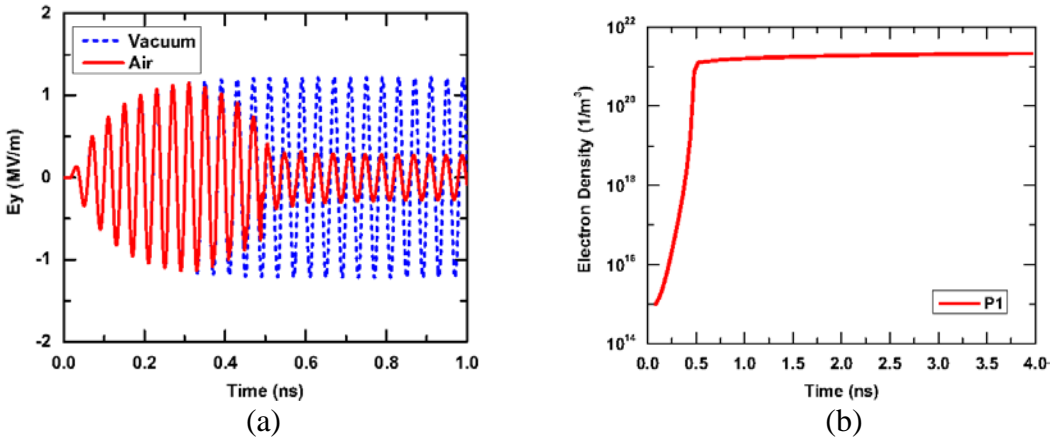


**Figure 9. (a) Comparison of the Temporal Response of the Electric Fields Recorded at P2 in Both Cases; (b) Temporal Evolution of the Electron Density Recorded at P1 in the Air Case**

To obtain a better understanding of the physical process, the spatial and temporal evolution of the electron density distribution is presented. Shown in Figure 10 is the electron density distribution in the air aperture at 0.28 ns. From its variation in the vertical direction shown in Figure 10(a), two peaks near the boundaries are observed, which is due to the edge singularity

that enhances the electric field near these two boundaries. To satisfy the Dirichlet boundary condition at the two boundaries, the electron density has to have very large density gradients around the boundaries, which need to be resolved with high spatial resolution. From Figure 10(b), the electron density distribution in the horizontal direction is almost sinusoidal except for a small shift towards the right, which is due to the nonuniform field distribution that results in different ionization rate along this direction. A two dimensional snapshot of the electron density at 0.28 ns is given in Figure 10(c) to provide a whole picture of the density distribution.

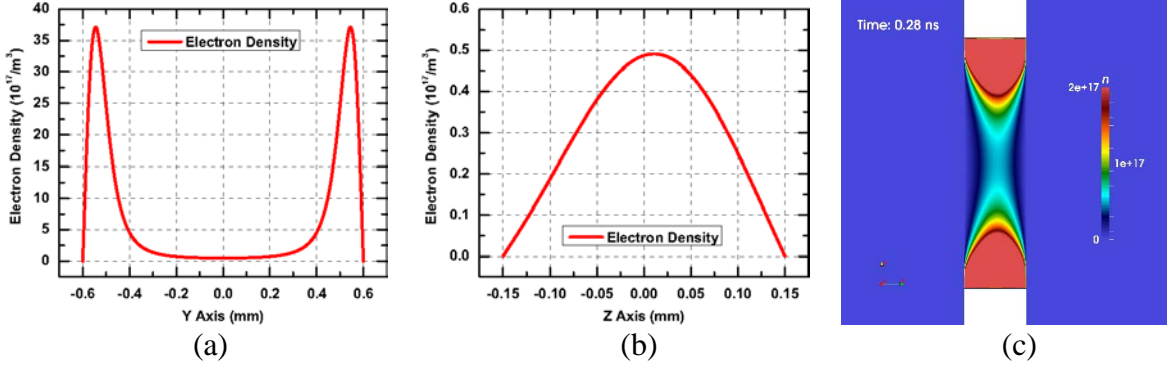


**Figure 10. Electron Density Distribution in the Air Aperture at 0.28 ns. (a) One Dimensional Distribution Along y Direction; (b) One Dimensional Distribution Along z Direction; (c) Two Dimensional Snapshot**

Spatial and temporal evolution of the electron density  $n$  and the effective field  $E_{\text{eff}}$  from 0.28 ns to 4.00 ns is presented in Figure 11 in terms of two dimensional snapshots once every electromagnetic period ( $1/25 \text{ GHz} = 0.04 \text{ ns}$ ). At 0.28 ns [Figure 11(a)], the electron density is too low to disturb the incident field, and the effective field reaches its maximum at four corners (hot spots) of the air aperture due to the edge singularity. These four hot spots lead to faster ionization and result in the four areas with higher electron density that can be observed from Figure 11(b) at 0.32 ns. These four plasma areas in return begin to shield the electromagnetic field within the areas and in the same time radiate at their boundaries secondary fields that enhance the incident fields, resulting smaller effective field within the plasma bulk and new hot spots around it. The new hot spots ionize more air that forms new areas of plasma bulk which shields more electromagnetic fields and generates newer hot spots [Figure 11(c)]. Such a process keeps on going until about 0.5 ns, when the ionized plasma pattern is fully developed and the electromagnetic field is shielded in the entire air aperture, resulting in a significant magnitude drop of the observed electric fields at both P1 and P2 points, as those presented in Figure 8(b) and Figure 9(a).

After 0.5 ns, the ionization of the neutral air becomes very slow. Instead, the dominant physical mechanism changes from ionization to diffusion, where the electron diffuses from the higher-density regions to lower-density regions. Specifically, the plasma front exhibits the free diffusion with a high electron diffusion coefficient, and the plasma bulk exhibits the ambipolar diffusion which has a much lower ambipolar diffusion coefficient. As a result, from 0.60 ns [Figure 11(i)] to 4.00 ns [Figure 11(j)], the overall pattern of the plasma formation does not change

significantly due to the slow ambipolar diffusion. But the boundaries of the plasma regions become blurred and smoother, because of the free electron diffusion near the plasma boundaries that inject the lower-density regions with more electrons.

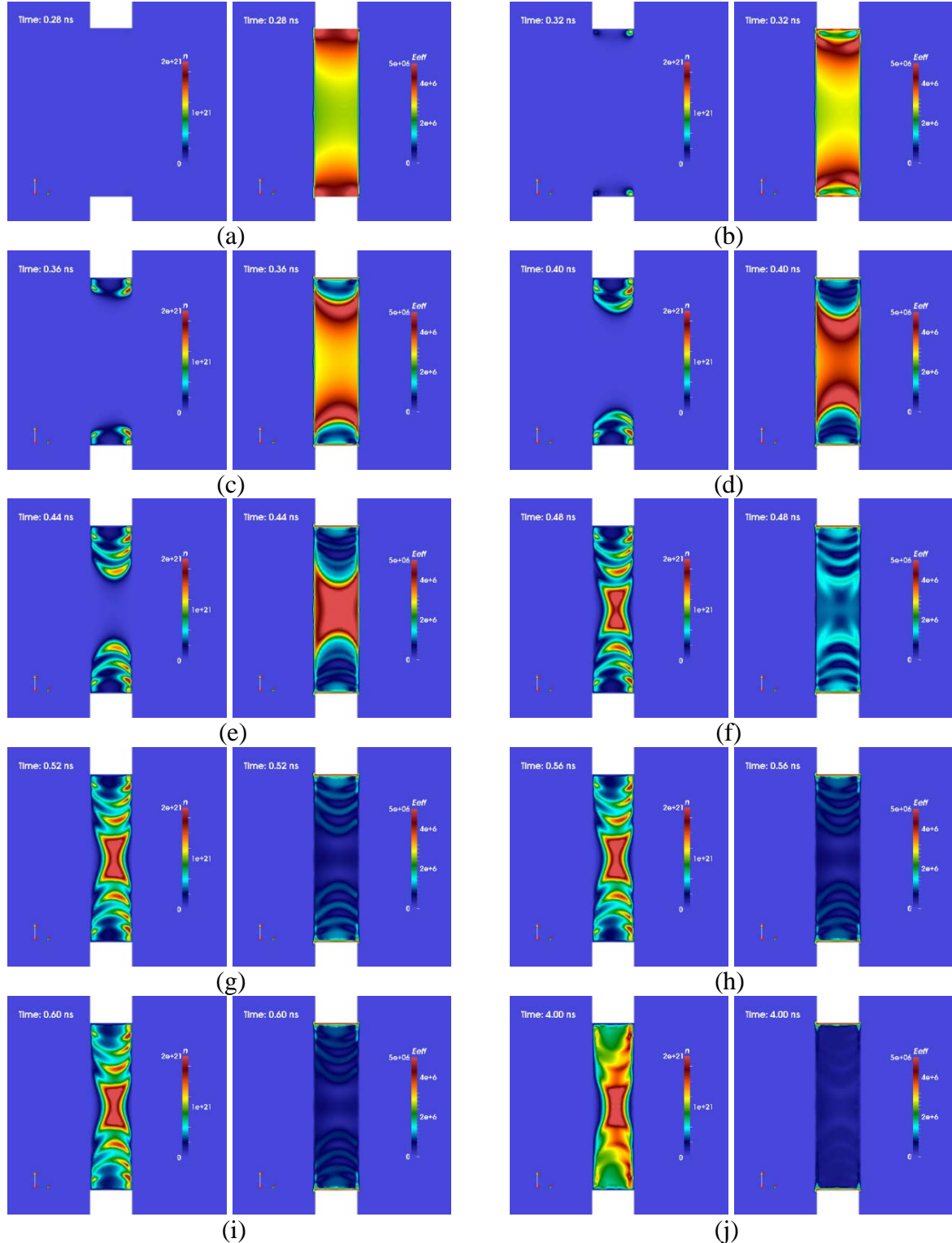


**Figure 11. Snapshots of the Time Evolution of the Electron Density and the Effective Electric Field in the Air Aperture at (a) 0.28 ns, (b) 0.32 ns, (c) 0.36 ns, (d) 0.40 ns, (e) 0.44 ns, (f) 0.48 ns, (g) 0.52 ns, (h) 0.56 ns, (i) 0.60 ns, and (j) 4.00 ns, Respectively**

From this example, it is clear that the methodology developed in this work is fully capable to capture the dominant physical mechanism (ionization versus diffusion) and provide deeper insight to the physical phenomenon and process.

### 4.3 Reproduction of the Microwave Streamer

In the last example, the generation of the microwave streamer is considered. As shown in Figure 12, the microwave streamer discharge demonstrates the elongation effect of a plasma bulk under the excitation of a standing electric field. Under the combined effect of diffusion, ionization, attachment, and recombination, the plasma bulk will grow longer from its initial shape, for example, a Gaussian distribution, in the direction of the externally applied electric field. The generation of the microwave streamer is experimentally observed and reported in [42].

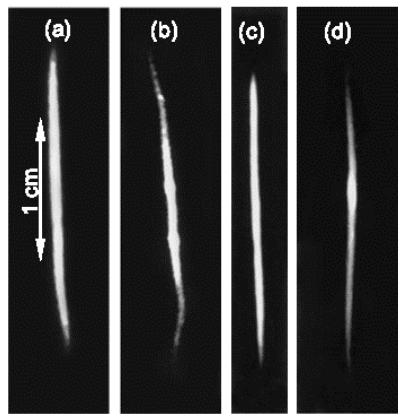


**Figure 12. The Microwave Streamer Discharge Recorded in Experiments. Streamer Discharges in Air at (a) 480 torr and (b) 760 torr. Streamer Discharges in Hydrogen at (c) 480 torr and (d) 1000 torr [42]**

#### 4.3.1 Physics Involved

Shown in Figure 13 is the effective ionization frequency and electron free diffusion coefficient as functions of reduced effective field. When the effective field is below the critical value (shown as the vertical dashed line), the attachment effect dominates over the ionization effect, while when the effective field is higher than the critical value, the ionization frequency increases dramatically and becomes dominant. The diffusion coefficient is also a function of the reduced effective field, but it increases much slower compared to the ionization frequency.

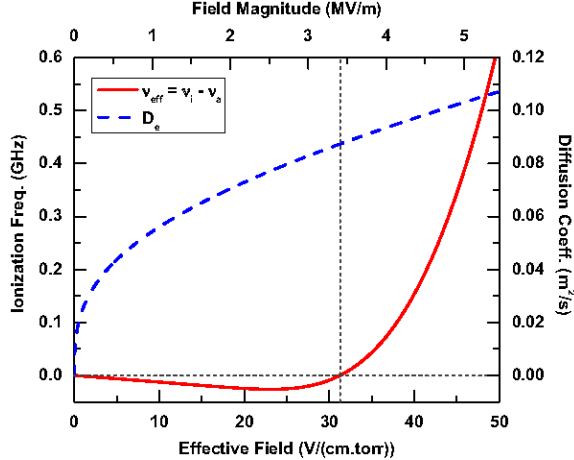


**Figure 13. Effective Ionization Frequency and Electron Diffusion Coefficient as Functions of Effective Field**

### 4.3.2 Numerical Settings

In the experiment, for the air breakdown to begin, a highly intensive Gaussian beam is shined into an air chamber, which initiates the air breakdown at its focal point. In the numerical simulation, the simulation domain is set as a 3D cylindrical region filled with 760-torr air, with all its boundaries set as ABC for the electromagnetic waves and homogeneous Dirichlet boundary condition for the plasma. Instead of the Gaussian beam, a 110-GHz, 6-MV/m, horizontally polarized standing wave is launched in the solution domain with the maximum value of the standing wave located along the center line (the symmetric axis) of the cylindrical air box, and a seed electron bulk is placed at the center point of the air box, which has a density distribution as a Gaussian dot with the maximum density set as  $10^{15}/\text{m}^3$  and the standard deviation set as  $100 \mu\text{m}$ , as shown in Figure 14.

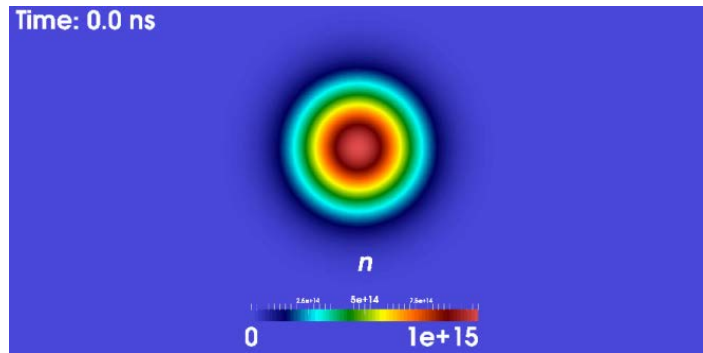
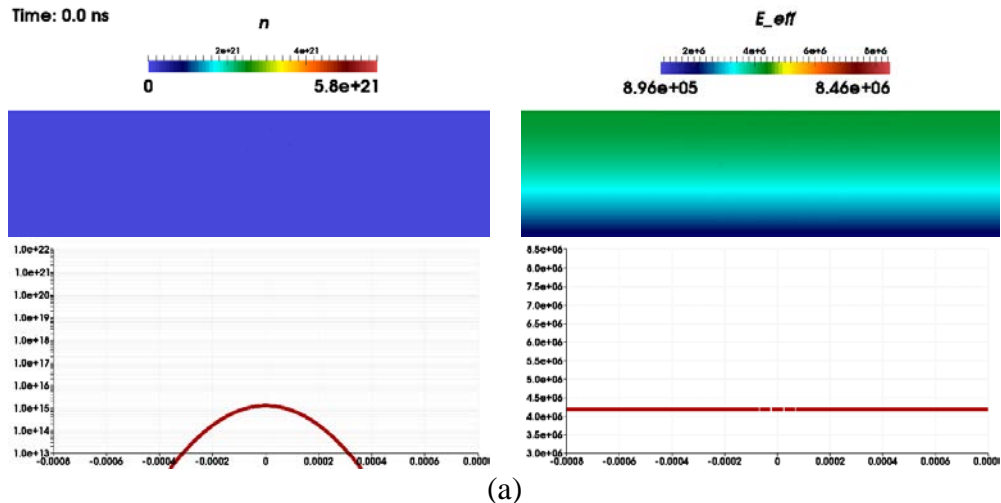


**Figure 14. The Initial Condition of the Electron Distribution, a Gaussian Dot**

### 4.3.3 Numerical Results and Analysis

The spatial and temporal evolution of the microwave streamer is shown in Figure 15 at multiple time steps. From these figures, it can be seen that from the initial time step [Figure 15(a)] to about 12.0 ns [Figure 15(b)], the shape of the plasma bulk remains almost the same, while the electron density increases from the initial  $10^{15}/\text{m}^3$  to about  $10^{21}/\text{m}^3$  due to ionization of neutral gas into the plasma. Since the secondary fields radiated by the plasma oscillation are still too weak to disturb the incident waves, the effective fields shown in these two figures are almost straight lines with similar magnitude, indicating that the effective field is dominated by the incident standing wave. From 12.0 ns, the electron density grows to a significant level such that its radiated fields start to interact with the incident waves, which results in the increase of the effective fields at the plasma front in the direction of the electric field (the horizontal direction in the figures) and the decrease in between of these two peaks of the effective fields due to the plasma shielding to the electromagnetic fields, as can be observed from Figure 15(c) at 14.0 ns. The difference of the effective fields in the plasma region result in different ionization frequencies and diffusion coefficients, which leads to a faster ionization rate and diffusion velocity at the two tips of the plasma region compared with the inside of the plasma bulk, causing the electron density at these regions to increase faster than that at other regions. This makes the plasma bulk change its shape and grow longer in the horizontal direction. Such a process continues and generates even sharper peaks of the effective fields at the plasma front and even lower magnitude of the effective fields inside the plasma bulk, and therefore, the elongation of the plasma bulk continues, which eventually produces the so-called microwave streamer in the direction of the incident electric field as can be seen in Figure 15(d).



(a)

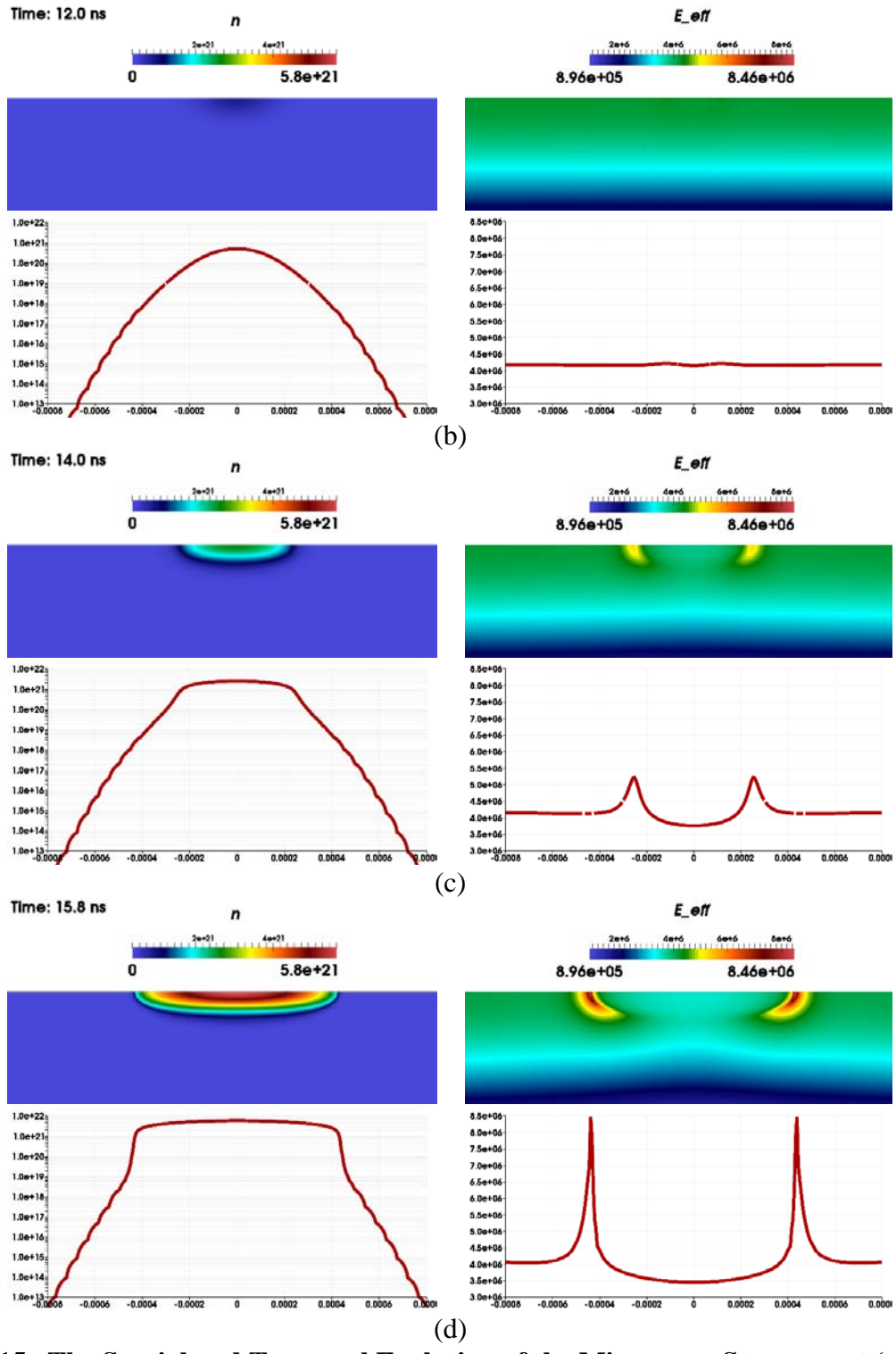


**Figure 15. The Spatial and Temporal Evolution of the Microwave Streamer at (a) 0.0 ns, (b) 12.0 ns, (c) 14.0 ns, and (d) 15.8 ns, Respectively. In Each Set of Plot, the Upper Two Figures Show the Electron Density and the Effective Field Distributions in a 2D Cut, and the Lower Two Figures Show the Corresponding Distributions as 1D Curves Along the Center Line (the Symmetric Axis)**

The electron density and the secondary electric field distribution at 15.8 ns are shown in Figure 16(a) and (b), respectively. From Figure 16(a), it is clear that the plasma is elongated in the direction of the incident electric field. From Figure 16(b), the plasma shielding to the electromagnetic waves can be seen clearly. It can also be observed that the secondary electric field is concentrated at the two tips of the plasma bulk, which is because the electric field radiated by a small electric dipole (a highly oscillating electron) in the plasma front cannot be cancelled by the electric fields radiated by its neighboring dipoles due to the imbalanced electron density resulted from the high electron density gradient at the plasma front [refer to Figure 15(d)]. The radiation and shielding of the electromagnetic fields by the oscillating plasma can be observed in Figure 16(c), where the two plots are presented on top of each other.

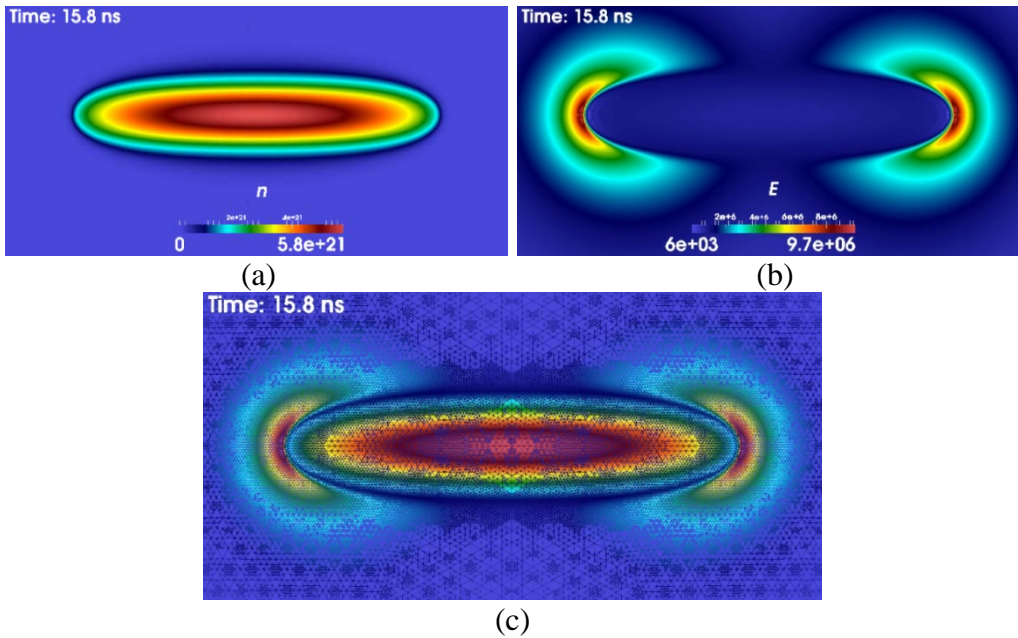


**Figure 16. (a) Electron Density, (b) Secondary Electric Field Distribution, and (c) Combination View of the Electron Density and the Secondary Electric Field Generated by the Electron Plasma at 15.8 ns**

As pointed out in the preceding sections, the field continuity in all directions is very important in order to obtain the correct plasma coefficients in the simulation. This can be guaranteed by the use of the nodal DGTd method. Presented in Figure 17 are the  $y$  and  $z$  components of the secondary electric field radiated by the electron plasma at 15.8 ns, which demonstrate the field continuity in all directions throughout the simulation domain.

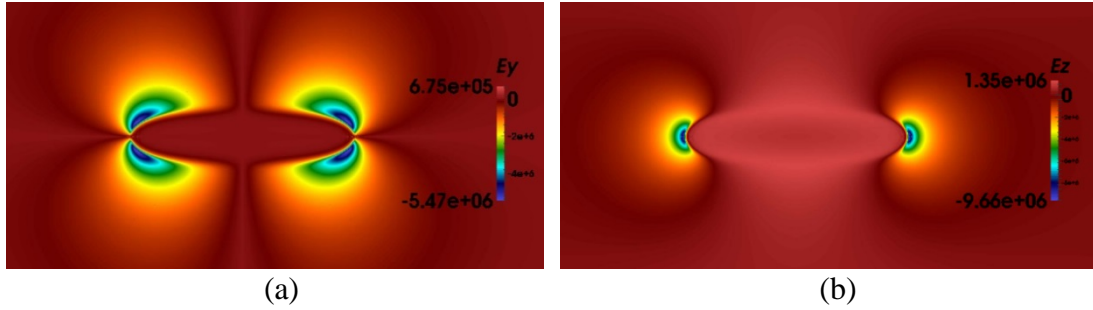


**Figure 17.** The (a) y and (b) z Components of the Secondary Electric Field Radiated by the Electron Plasma at 15.8 ns, Which Demonstrate the Field Continuity in all Directions Throughout the Simulation Domain. The x Component is Zero in the Plane of Observation and is Not Shown

Figure 18 demonstrates the change of polynomial orders at the initial and final time steps. Apparently, the proposed dynamic  $p$ -adaption algorithm can track the plasma front when it propagates and determine the appropriate polynomial order for different positions at different time steps. With the aid of the dynamic  $p$ -adaption algorithm, the computational time can be reduced by two orders of magnitude compared with that using a uniform polynomial order throughout the entire computational domain.

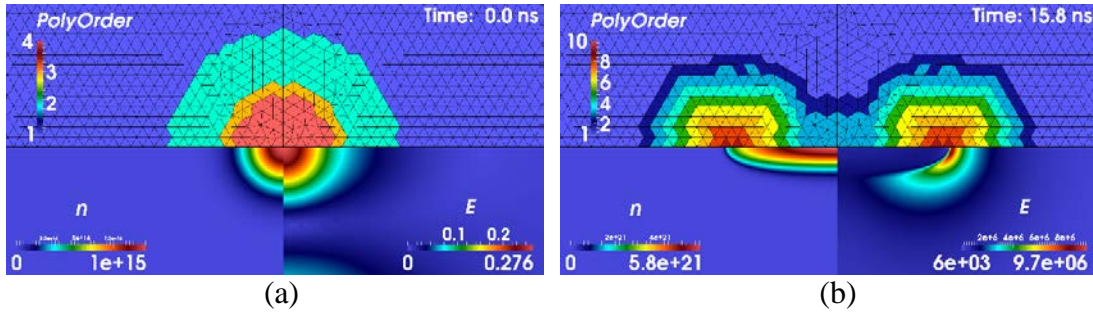


**Figure 18.** Dynamic  $p$ -Adaption During Simulation. The Upper Half of the Two Figures Show the Polynomial Orders in the Computational Domain, the Lower Left and Lower Right of the Two Figures are the Electron Density and Electric Field Magnitude, Respectively. (a) 0.0 ns; (b) 15.8 ns

## 5.0 CONCLUSIONS

In this report, a highly accurate and efficient simulation tool is developed for the multi-physics and multiscale modeling and simulation of the electromagnetic-plasma interaction and the high-power microwave breakdown in air. The coupled electromagnetic-plasma system consists of two Maxwell's equations, a particle kinetic equation, and a particle diffusion equation. The nonlinear dependence of the plasma parameters on the electromagnetic fields makes the entire system highly nonlinear. In order to deal with such a multi-physics, multiscale, and nonlinear system, the nodal DGTD method is adopted together with the high-order Runge-Kutta method in the

solution of the hyperbolic Maxwell's equations and the parabolic diffusion equation. To obtain a better computational efficiency, a dynamic  $p$ -adaption algorithm is proposed and a GPU-accelerated algorithm is implemented. With the development of all the advanced computational techniques, the high-power microwave breakdown problems can be successfully simulated, which provides deeper insight and better understanding of the physical phenomenon and the breakdown process. Further effort is being taken to test on the nodal DGTD for modeling of various devices involving dielectrics and conductors where a normal discontinuity at a material interface is present.

## 6.0 REFERENCES

- [1] S. H. Gold and G. S. Nusinovich, "Review of high-power microwave source research," *Rev. Sci. Instrum.*, vol. 68, no. 11, pp. 3945-3974, Nov. 1997.
- [2] J. Benford, and G. Benford, "Survey of pulse shortening in high-power microwave sources," *IEEE Trans. Plasma Sci.*, vol. 25, no. 2, pp. 311-317, Apr. 1997.
- [3] A. Neuber, J. Dickens, D. Hemmert, H. Krompholz, L. L. Hatfield, and M. Kristiansen, "Window breakdown caused by high-power microwaves," *IEEE Trans. Plasma Sci.*, vol. 26, no. 3, pp. 296-303, June 1998.
- [4] D. Hemmert, A. A. Neuber, J. Dickens, H. Krompholz, L. L. Hatfield, and M. Kristiansen, "Microwave magnetic field effects on high-power microwave window breakdown," *IEEE Trans. Plasma Sci.*, vol. 28, no. 3, pp. 472-477, June 2000.
- [5] J. Foster, S. Beeson, M. Thomas, J. Krile, H. Krompholz, and A. Neuber, "Rapid formation of dielectric surface flashover due to pulsed high power microwave excitation," *IEEE Trans. Dielectr. Electr. Insul.*, vol. 18, no. 4, pp. 964-970, Aug. 2011.
- [6] R. A. Anderson and J. P. Brainard, "Mechanism of pulsed surface flashover involving electron stimulated desorption," *J. Appl. Phys.*, vol. 51, p. 1414, 1980.
- [7] A. S. Pillai and R. Hackam, "Surface flashover of solid dielectric in vacuum," *J. Appl. Phys.*, vol. 53, p. 2983, 1982.
- [8] R. A. Kishek and Y. Y. Lau, "Interaction of multipactor discharge and R. F. circuits," *Phys. Rev. Lett.*, vol. 75, p. 1218, 1995.
- [9] R. A. Kishek and Y. Y. Lau, "A novel phase focusing mechanism in multipactor discharge," *Phys. Plasmas*, vol. 3, p. 1481, 1996.
- [10] J. T. Krile, A. A. Neuber, H. G. Krompholz, and T. L. Gibson, "Monte Carlo simulation of high power microwave window breakdown at atmospheric conditions," *Appl. Phys. Lett.*, vol. 89, 201501, 2006.
- [11] P. Zhao, C. Liao, W. Lin, L. Chang, and H. Fu, "Numerical studies of the high power microwave breakdown in gas using the fluid model with a modified electron energy distribution function," *Phys. Plasmas*, vol. 18, pp. 102-111, 2011.
- [12] J. M. Jin, *The Finite Element Method in Electromagnetics, Second Edition*. New York: Wiley, 2002.
- [13] C. E. Baumann and J. T. Oden, "A discontinuous  $hp$  finite element method for convection-diffusion problems," *Comput. Methods Appl. Mech. Engrg.*, vol. 175, pp. 311-341, 1999.
- [14] B. Cockburn, G. E. Karniadakis, and C.-W. Shu, "The development of discontinuous Galerkin methods," in *Discontinuous Galerkin Methods. Theory, Computation and*

- Applications*, B. Cockburn, G. E. Karniadakis, and C.-W. Shu, eds., Lecture Notes in Comput. Sci. Engrg. 11, Springer-Verlag, New York, 2000, pp. 3–50.
- [15] B. Cockburn, S. Y. Lin, and C.-W. Shu, “TVB Runge-Kutta local projection discontinuous Galerkin finite element method for conservation laws III: One dimensional systems,” *J. Comput. Phys.*, vol. 84, pp. 90–113, 1989.
  - [16] B. Cockburn and C.-W. Shu, “TVB Runge-Kutta local projection discontinuous Galerkin finite element method for scalar conservation laws II: General framework,” *Math. Comp.*, vol. 52, pp. 411–435, 1989.
  - [17] B. Cockburn and C.-W. Shu, “The local discontinuous Galerkin method for time-dependent convection-diffusion systems,” *SIAM J. Numer. Anal.*, vol. 35, pp. 2440–2463, 1998.
  - [18] B. Cockburn and C.-W. Shu, “The Runge-Kutta discontinuous Galerkin finite element method for conservation laws V: Multidimensional systems,” *J. Comput. Phys.*, vol. 141, pp. 199–224, 1998.
  - [19] J. S. Hesthaven and T. Warburton, *Nodal Discontinuous Galerkin Methods Algorithms: Analysis, and Applications*, New York: Springer, 2008.
  - [20] T. Lu, P. W. Zhang, and W. Cai, “Discontinuous Galerkin methods for dispersive and lossy Maxwell’s equations and PML boundary conditions,” *J. Comput. Phys.*, vol. 200, no. 2, pp. 549–580, Nov. 2004.
  - [21] S. D. Gedney, C. Luo, J. A. Roden, R. D. Crawford, B. Guernsey, J. A. Miller, T. Kramer, and E. W. Lucas, “The discontinuous Galerkin finite-element time-domain method solution of Maxwell’s equations,” *Appl. Comput. Electromag. Soc. J.*, vol. 24, no. 2, pp. 129–142, Apr. 2009.
  - [22] J. A. Bittencourt, *Fundamentals of Plasma Physics*. New York: Springer-Verlag, 2004
  - [23] J. H. Yee, D. J. Mayhall, G. E. Sieger, and R. A. Alvarez, “Propagation of intense microwave pulses in air and in a waveguide,” *IEEE Trans. Antennas Propag.*, vol. 39, no. 9, pp. 1421–1426, 1991.
  - [24] W. V. V. Roosbroeck, “Theory of flow of electrons and holes in Germanium and other semiconductors,” *Bell System Technical Journal*, vol. 29, pp. 560–607, 1950.
  - [25] K. Blotekjaer, “Transport equations for electrons in two-valley semiconductors,” *IEEE Trans. Electron Devices*, vol. 17, no. 1, pp. 38–47, 1970.
  - [26] C. Ringhofer, C. Schmeiser, and A. Zwiglmayr, “Moment methods for the semiconductor Boltzmann equation on bounded position domains,” *SIAM Journal of Numerical Analysis*, vol. 39, no. 3, pp. 1078–1095, 2001.
  - [27] T. Grasser, T. W. Tang, H. Kosina, and S. Selberherr, “A review of hydrodynamic and energy transport models for semiconductor device simulation,” *Proc. IEEE*, vol. 91, no. 2, pp. 251–274, 2003.
  - [28] T. Grasser, H. Kosina, M. Gritsch, and S. Selberherr, “Using six moments of Boltzmann’s transport equation for device simulation,” *J. Appl. Phys.*, vol. 90, no. 5, pp. 2389–2396, 2001.
  - [29] J. P. Boeuf, B. Chaudhury, G. Q. Zhu, “Theory and modelling of self-organization and propagation of filamentary plasma arrays in microwave breakdown at atmospheric pressure,” *Phys. Rev. Lett.*, vol. 104, 015002, 2010.
  - [30] B. Chaudhury, J. P. Boeuf, G. Q. Zhu, “Pattern formation and propagation during microwave breakdown,” *Phys. Plasmas*, vol. 17, 123505, 2010.

- [31] B. Chaudhury, J. P. Boeuf, “Computational studies of filamentary pattern formation in a high power microwave breakdown generated air plasma,” *IEEE Trans. Plasma Sci.*, vol. 38, p. 2281, 2010.
- [32] G. Q. Zhu, J. P. Boeuf, B. Chaudhury, “Ionization-diffusion plasma front propagation in a microwave field,” *Plasma Sources Sci. Technol.*, vol. 20, 035007, 2011.
- [33] A. Hamiaz, R. Klein, X. Ferrieres, O. Pascal, J. P. Boeuf, J. R. Poirier, “Finite volume time domain modelling of microwave breakdown and plasma formation in a metallic aperture,” *Comput. Phys. Commun.*, vol. 183, pp. 1634–1640, 2012.
- [34] M. Zhang and C.-W. Shu, “An analysis of three different formulations of the discontinuous Galerkin method for diffusion equations,” *Math. Models Methods Appl. Sci.*, vol. 13, p. 395, 2003.
- [35] J. C. Butcher, *Numerical Methods for Ordinary Differential Equations*, Wiley, 2003.
- [36] S. Gottlieb, D. Ketcheson, and C. W. Shu, *Strong Stability Preserving Runge-Kutta and Multistep Time Discretizations*, New Jersey: World Scientific, 2011.
- [37] C. W. Shu, “Total-variation diminishing time discretizations,” *SIAM Journal on Scientific and Statistical Computing*, vol. 9, pp. 1073-1084, 1988.
- [38] C. W. Shu and S. Osher, “Efficient implementation of essentially non-oscillatory shock-capturing schemes,” *J. Comput. Phys.*, vol. 77, pp. 439-471, 1988.
- [39] D. B. Kirk and W. W. Hwu, *Programming Massively Parallel Processors*. Burlington, MA, USA: Morgan Kaufmann, 2010.
- [40] H.-T. Meng and J. M. Jin, “Acceleration of the dual-field domain decomposition algorithm using MPI-CUDA on large-scale computing systems,” *IEEE Trans. Antennas Propagat.*, vol. 62, no. 9, pp. 4706-4715, Sept. 2014.
- [41] H.-T. Meng, B.-L. Nie, S. Wong, C. Macon, and J. M. Jin, “GPU accelerated finite element computation for electromagnetic analysis,” *IEEE Antennas Propagat. Mag.*, vol. 56, no. 2, pp. 39-62, April 2014.
- [42] V. S. Barashenkov, L. P. Grachev, I. I. Esakov, B. F. Kostenko, K. V. Khodataev, and M. Z. Yur’ev. “Threshold for a cumulative resonant microwave streamer discharge in a high-pressure gas,” *Tech. Phys.*, vol. 45, no. 11, pp. 1406–1410, 2000.

## DISTRIBUTION LIST

DTIC/OCP  
8725 John J. Kingman Rd, Suite 0944  
Ft Belvoir, VA 22060-6218                    1 cy

AFRL/RVIL  
Kirtland AFB, NM 87117-5776                    1 cy

Official Record Copy  
AFRL/RDHE/Andrew Greenwood                    1 cy

This page intentionally left blank.